



1
2
3
4
5
6
7
8
9
10
11
12
13
14
15
16
17
18
19
20
21
22
23
24
25
26
27
28
29
30
31
32
33
34
35
36
37
38
39
40
41
42
43

**Observations of Shoaling Internal Wave Transformation Over a Gentle Slope in
the South China Sea**

Steven R. Ramp¹, Yiing Jang Yang², Ching-Sang Chiu³, D. Benjamin Reeder³, and
Frederick L. Bahr⁴

[1] {Soliton Ocean Services LLC, Falmouth, MA 02540}
[2] {Institute of Oceanography, National Taiwan University, Taipei, Taiwan}
[3] {Dept. of Oceanography, Naval Postgraduate School, Monterey, CA 93943}
[4] {Monterey Bay Aquarium Research Institute, Moss Landing, CA 95039}
Correspondence to: S. R. Ramp (sramp@solitonocean.com)



45 **Abstract**

46

47

48

49

50

51

52

53

54

55

56

57

58

59

60

61

62

63

64

65

66

67

68

Four oceanographic moorings were deployed across the South China Sea continental slope near 21.85°N, 117.71°E, from May 30 to July 18, 2014 for the purpose of observing high-frequency nonlinear internal waves (NLIWs) as they shoaled across a rough, gently sloping bottom. Individual waves required just two hours to traverse the array and could thus easily be tracked from mooring-to-mooring. In general, the amplitude of the incoming NLIWs was a good match with the fortnightly tidal envelope in the Luzon Strait, lagged by 48.5 hours, and were smaller than the waves observed 50 km to the southwest near the Dongsha Plateau. The now-familiar type a-waves and b-waves were observed, with the b-waves always leading the a-waves by 6-8 hours. Most of the waves were remotely generated, but a few of the b-waves formed locally via convergence and breaking at the leading edge of the upslope internal tide. Waves incident upon the array with amplitude less than 50 m and energy less than 100 MJ m⁻¹ propagated adiabatically upslope with little change of form. Larger waves formed packets via wave dispersion. For the larger waves, the kinetic energy flux decreased sharply upslope between 342 m to 266 m while the potential energy flux increased slightly, causing an increasing ratio of potential-to-kinetic energy as the waves shoaled. The results are in rough agreement with recent theory and numerical simulations of shoaling waves.



69 **1 Introduction**

70 Considerable field work has now been dedicated to observing and understanding
71 the very large amplitude, high-frequency nonlinear internal waves (NLIW) in the
72 northeastern South China Sea (SCS). It has now been well established that the
73 waves emerge from an impressive internal tide which is generated by the flux of the
74 barotropic tide across the two ridges in the Luzon Strait [Buijsman et al., 2010a,
75 2010b; Zhang et al., 2011]. Both tidal conversion and dissipation are high around
76 the ridges [Alford et al., 2011], but adequate energy survives to escape the ridges
77 and propagate WNW across the sea. As they do so, the internal tides steepen
78 nonlinearly until eventually the NLIW are formed [Farmer et al., 2009; Li and
79 Farmer, 2011; Alford et al., 2015]. The longitude where this takes place depends on
80 the details of the forcing and stratification but based on satellite imagery it is not
81 until at least $120^{\circ} 30'E$, roughly 50 km west of the western (Heng-Chun) ridge
82 [Jackson, 2009]. This longitude is hypothesized to be the minimum distance/time
83 required for the internal tide to nonlinearly steepen and break, or perhaps the first
84 point where tidal beams intersect the sea surface west of the western ridge. Once
85 the NLIW have formed, they propagate WNW across the deep SCS basin with
86 remarkably little change of form [Alford et al., 2010; Ramp et al., 2010]. Once the
87 waves start to shoal on the continental slope however, roughly between 1000m to
88 150m depth, the changes are quite dramatic. Wave refraction due to the shallower
89 depth and changing stratification tends to align the wave crests with the local
90 topography. Incident waves which were initially solitary may form packets via
91 wave breaking or dispersion [Vlasenko and Hutter, 2002; Vlasenko and Stashchuk,
92 2007; Lamb and Warn-Varnas, 2015]. Some very large waves may split into two
93 smaller waves [Small 2001a, 2001b; Ramp, 2004]. When the wave's orbital velocity
94 exceeds the propagation speed, usually between 300m - 150m depth, the largest
95 waves may break and form trapped cores that transport mass and nutrients
96 onshore [Farmer et al., 2011; Lien et al., 2012; Lien et al., 2014; Chang et al., 2021].
97 Still farther onshore where the upper layer thickness exceeds the lower, the
98 depression waves are transformed into elevation waves [Orr and Mignerey, 2003;
99 Duda et al., 2004; Ramp et al., 2004; Liu et al., 2004]. The elevation waves
100 presumably continue propagating WNW towards shore and dissipate in shallow
101 water, but observations to the west of this point are scarce.

102
103 Two types of NLIWs, called a-waves and b-waves, have been repeatedly observed, a
104 parlance first coined by Ramp et al. [2004]. Based on the Asian Seas International
105 Acoustics Experiment (ASIAEX) results, the a-waves consisted of rank-ordered
106 packets that arrived at the same time every day and were generally larger than the
107 b-waves, which were usually solitary and arrived one hour later each day. It has
108 subsequently been shown via longer data sets that the timing is not universal and
109 that b-waves may sometimes be larger than a-waves. The correct manner of
110 classification is likely via their generating mechanism and location, but with regard
111 to this much controversy still remains. All agree that the waves stem from the
112 Luzon Straits, where the barotropic tide has a large fortnightly envelope, a strong
113 diurnal variation, and is asymmetric with stronger tides on ebb (towards the



114 Pacific) than on flood (towards the SCS). Some authors assert that both types of
115 waves are released on flood, with a-waves formed on the strong beat and b-waves
116 on the weak beat [Vlasenko et al., 2012]. Others find both types generated on ebb,
117 with a-waves formed at the east ridge and b-waves at the west ridge [Chen et al.,
118 2013]. A third school of thought finds the a-waves formed on the larger of the two
119 ebb tides and the b-waves on the larger flood [Alford et al., 2010; Ramp et al., 2010].
120 Finally, both types of waves may be spawned by the same tidal beat but at different
121 locations in the strait [Du et al., 2008; Zhang et al., 2011; Ramp et al., 2019]. A
122 resolution is desirable not only for its intrinsic scientific worth, but also to improve
123 the accuracy of NLIW prediction schemes presently being implemented in the SCS.
124

125 The present study was motivated by the discovery of large ($h > 15\text{m}$, λ order 350m)
126 undersea sand dunes on the sea floor along a transect southeastward from 21.93°N,
127 117.53°E in the northeastern South China Sea [Reeder et al., 2010]. Subsequent
128 multi-beam echo surveys (MBES) during 2013 and 2014 revealed that the dunes
129 occupy at least the region spanning 21.8 to 21.9°N and 117.5 to 117.7°E (Figure 1).
130 This region is on the continental slope slightly northeast of the Dongsha Plateau.
131 The bottom slope in the dunes region is relatively slight with respect to steeper
132 bottom slopes progressing both offshore and onshore from there. The sand dunes
133 are of interest due to their impact on shallow-water acoustic propagation, and their
134 interaction with shoaling internal tides and NLIWs traveling WNW up the slope.
135 The acoustic issues are addressed in other papers emerging from the program.
136 Oceanographic questions of interest include: 1) How are NLIWs transformed as
137 they shoal over a gentle slope between 388m and 266m over the continental slope?
138 2) What are the physical mechanisms responsible for this transformation? and 3)
139 How does the increased bottom roughness in the dune field affect energy
140 dissipation in the shoaling internal tides and NLIWs, relative to other locations?
141 Geophysical problems of interest include: 4) What, if any, is the role of the NLIW in
142 sediment re-suspension and dune building? 5) What determines the spatial scales
143 of the dunes? and 6) Why are the dunes located where they are, and why are they
144 not observed elsewhere?
145

146 Towards this end, a pilot study was conducted during May 2013 followed by a major
147 field experiment during June 2014 to address the questions above. An array of
148 environmental and acoustic moorings was deployed from the R/V OCEAN
149 RESEARCHER 1 during June 1-12 and recovered from the R/V OCEAN RESEARCHER
150 5 during June 15-30, 2014 (Figure 1). While the moorings were in the water, a
151 number of CTD stations and near-bottom time series were obtained from the
152 research vessels to study the wave/bottom interactions. A second research vessel
153 (OCEAN RESEARCHER 3) conducted towed-source operations nearby. This paper
154 addresses how the high-frequency nonlinear internal waves were transformed
155 under shoaling, while the tidal dissipation and dune-building processes will be
156 addressed in separate works. The data and methods are described in section 2, the
157 NLIW arrival patterns and their relation to the source tides in section 3, and the



158 wave transformations and energy conservation in section 4. A summary and
159 conclusion section follows.

160

161 **2 Data and Methods**

162

163 An array of four oceanographic moorings were deployed across the continental
164 slope from 21.81°N, 117.86°E (386 m) to 21.89°N, 117.56°E (266 m) (Figure 1,
165 Table 1). The moorings labeled YPO2, YPO1, CPO, and RPO were separated by 4.10,
166 3.30, and 5.69 km respectively corresponding to wave travel times of 36.5, 30.3, and
167 56 min between moorings, such that individual waves could easily be identified and
168 traced across the array. Temperature and salinity were sampled at 60s intervals.
169 Instrument spacing ranged from 15 m to a maximum of 30 m in the vertical to
170 resolve internal wave amplitudes. Currents at RPO were sampled using three
171 downward looking 300 kHz ADCPs moored at 27 m, 105 m, and 184 m depth which
172 provided coverage of the entire water column except the upper 20 m. Currents at
173 CPO were also sampled using three 300 kHz ADCPs, one downward-looking unit
174 moored at 15 m depth, and an up/down pair at 264 m depth. Since the range of
175 these instruments was nominally 100 m, there was an unsampled region spanning
176 roughly 115 – 164 m depth at mooring CPO. Currents at YPO1 and YPO2 were
177 sampled using one 75 kHz and one 300 kHz ADCP. The 75 kHz instruments were
178 mounted downward looking in the top syntactic foam sphere at 20 m depth. The
179 300 kHz instruments were also mounted downward looking in cages at 300 m
180 depth. The 300 kHz instruments burst-sampled for 20 s every 90 s, while the 75
181 kHz instruments sampled once per second and were averaged to 90 s intervals
182 during post-processing. These sampling rates were adequate to observe the
183 shoaling NLIWs with no aliasing. A fifth mooring labeled “source” on roughly the
184 same isobath as CPO (Figure 1) sampled temperature only from 27 to 267 m. This
185 mooring was targeted for the same “trough” in the sand dune field as CPO to
186 examine along-crest acoustic propagation. It additionally proved useful to identify
187 the precise phasing and orientation of the internal wave crests in the along-slope
188 direction.

189

190 Continuous underway sampling of velocity and backscatter was achieved using the
191 ships’ hull mounted ADCPs and echo sounders. These were a narrow-band 150 kHz
192 ADCP system and EK500 on the OR1 and a 75 kHz Ocean Surveyor with fish finder
193 on the OR5. The ship’s radar images, which clearly showed the surface expression
194 of the NLIWs, were recorded once per minute throughout the cruises. MODIS ocean
195 color imagery for the region was collected and archived when available.

196

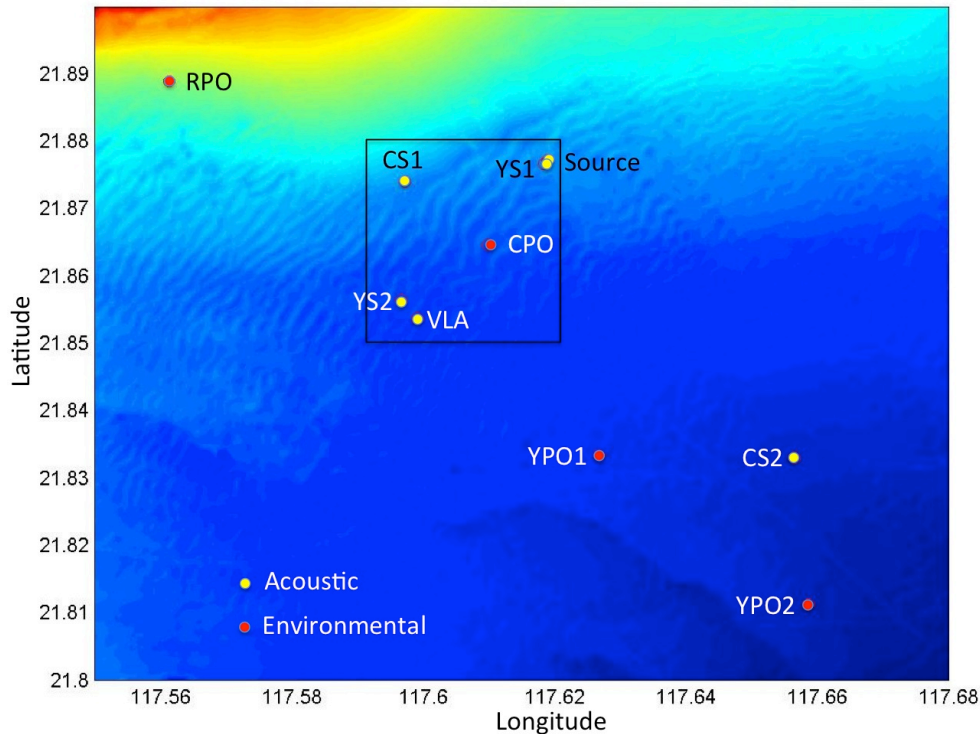
197 **3 Results**

198

199 *3.1 The Nature of the Dunes*

200

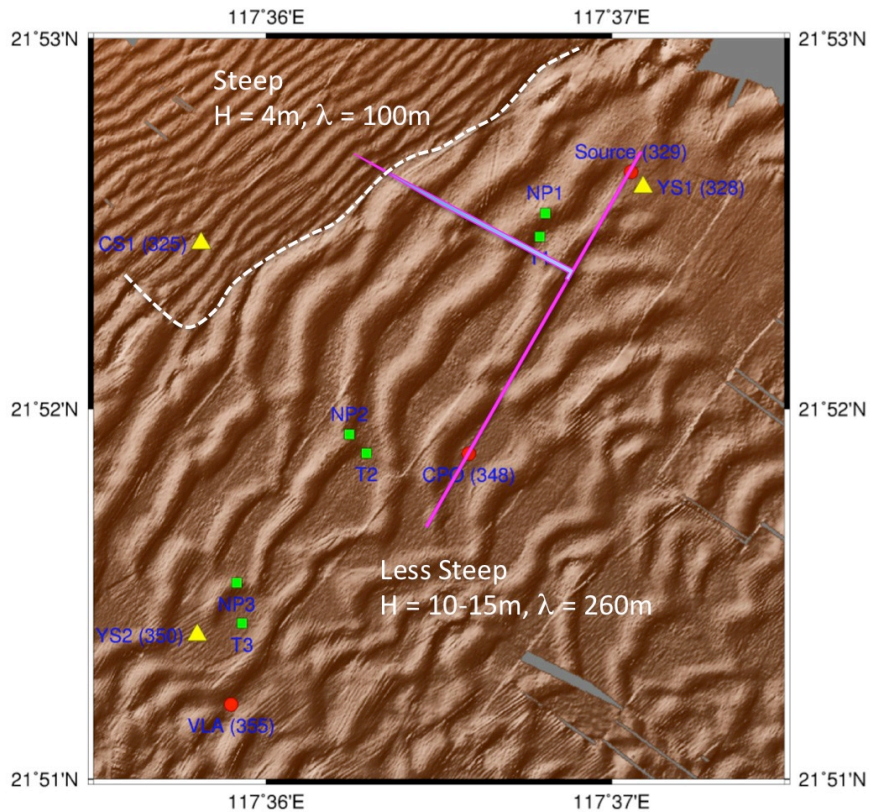
201 The stage is set by a zoomed-in view of the study region showing the seafloor sand
202 dunes as depicted by the MBES data (Figure 2). A change in the bottom slope forms
203 a very clear line of demarcation between lower (4 m) dunes with shorter (100 m)



204
205
206
207
208
209
210
211
212
213
214
215
216
217
218
219
220
221
222
223
224
225
226
227

Figure 1. Locator map for the Sand Dunes 2014 field experiment. This paper primarily concerns the environmental moorings indicated by the red dots, although temperature from the “source” mooring is also used. The mean bottom depth ranged from 388 m at YPO2 to 266 m at RPO. The sand dunes on the sea floor look like ripples in this image. The area within the black box is expanded in Figure 2.

wavelength and the larger (10-15 m) dunes with longer (260 m) wavelength. Dunes in these regions were nearly sinusoidal. Farther down the slope in water > 360m depth, the dunes were “parted” meaning the trough widths were much greater than the crest widths. Mooring RPO was located in the first region with steeper slope, CPO was in the second region of smaller slope and large sinusoidal dunes, and moorings YPO1 and YPO2 were in a region with similar mean bottom slope but parted dunes. Repeat MBES surveys indicated that during 2013-14, the dunes were stationary. Bottom sediment grabs revealed that the dunes were composed of sand and gravelly sand near the crests, and finer clayey and silty sand in the troughs. More details on the sediment characteristics may be found in a subsequent paper on dune formation. For purposes of this paper, the most important fact about the bottom is the sharp, clear change of bottom slope across the white dotted line (Figure 2) from $1:35 = .03 = 3\% = 2.0^\circ$ over the shallower part to $1:160 = .006 = 0.6\% = 0.3^\circ$ over the deeper part. These slopes are essential for comparing the observations to theory.



241
242
243

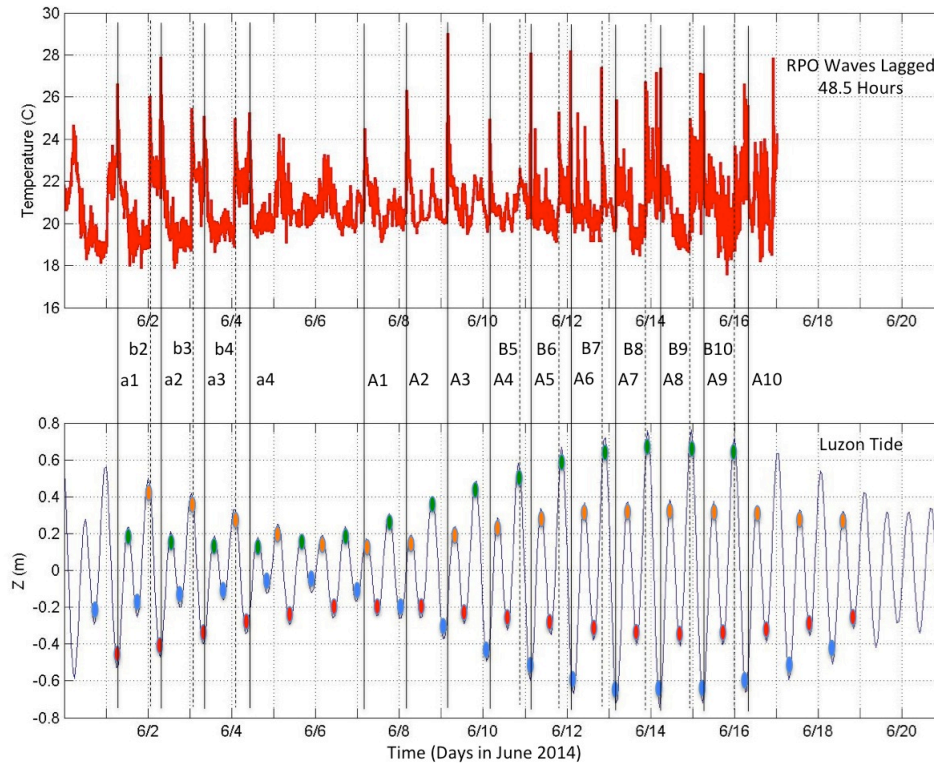
244 *Figure 2. The sea floor in the study region as observed by a multi-beam echo sounder*
245 *(MBES) survey during June 2014. The region is delineated by the black box in Figure 1.*
246 *The dotted white line indicates a sharp change in bottom slope, steeper towards the*
247 *northwest. The magenta arrow indicates the direction of propagation of the nonlinear*
248 *internal waves (NLIW) as determined by temperature sensors on moorings CPO and*
249 *“source.”*

250

251 (WISE/VANS) program, the mean propagation time from the east (Lan-Yu) ridge to
252 their mooring S7 (the same location as ASIAEX mooring S7) when averaged over an
253 entire year was 50.31 hours [Ramp et al., 2010]. Mooring RPO was slightly closer to
254 the ridge than S7, about 1.8 hours based on the local propagation time from CPO to
255 RPO. Thus, the time series of current and temperature from mooring RPO were
256 lagged back by 48.5 hours and compared to the model tidal heights from 20° 35'N,
257 121° 55'E on the east ridge.

258

259 The plot of the lagged temperature fluctuations at 75 m depth on mooring RPO vs.
260 the barotropic tidal heights at Luzon Strait reveals a number of interesting features
261 (Figure 3). The tides (lower panel) show the now familiar pattern of a large



262
263
264

265 *Figure 3. Wave arrival times at mooring RPO compared to the barotropic tidal beat in*
266 *the Luzon Strait. The temperature time series is from a single instrument moored near*
267 *75 m depth sampling at 60s intervals. The tidal heights were computed from the*
268 *TPX07.0 global tidal model at 20°35.4'N, 121°55.1'E in the strait between Batan and*
269 *Itbayat Island. The wave arrivals at RPO, indicated by sharp warm spikes in the*
270 *temperature profile due to thermocline depression, have been lagged back by 46.5*
271 *hours, the wave propagation time between the two sites. Solid vertical lines indicate*
272 *type-a (A) waves and the dotted lines are type-b (B) waves. Lower case is used to*
273 *delineate waves observed during the first fortnight and upper case the second. There*
274 *is no dynamical difference between the two. The colored dots indicate how the major*
275 *and minor tidal beats switched positions during the neap tide.*

276
277
278
279
280
281
282
283

fortnightly variation accompanied by a strong diurnal variability. This produced a
strong beat/weak beat pattern with amplitude only 0.2 m at neap tide but four
times greater (0.8 m) at spring. Note the position of the colored dots: The major and
minor peaks, marked by the red and blue dots on ebb and the orange and green dots
on flood, switched positions during the neap tide such that the weaker beat became
the stronger beat and vice-versa. This produced a corresponding shift in the wave
arrival times at the Sand Dunes moored array. Note that the stronger flood beat

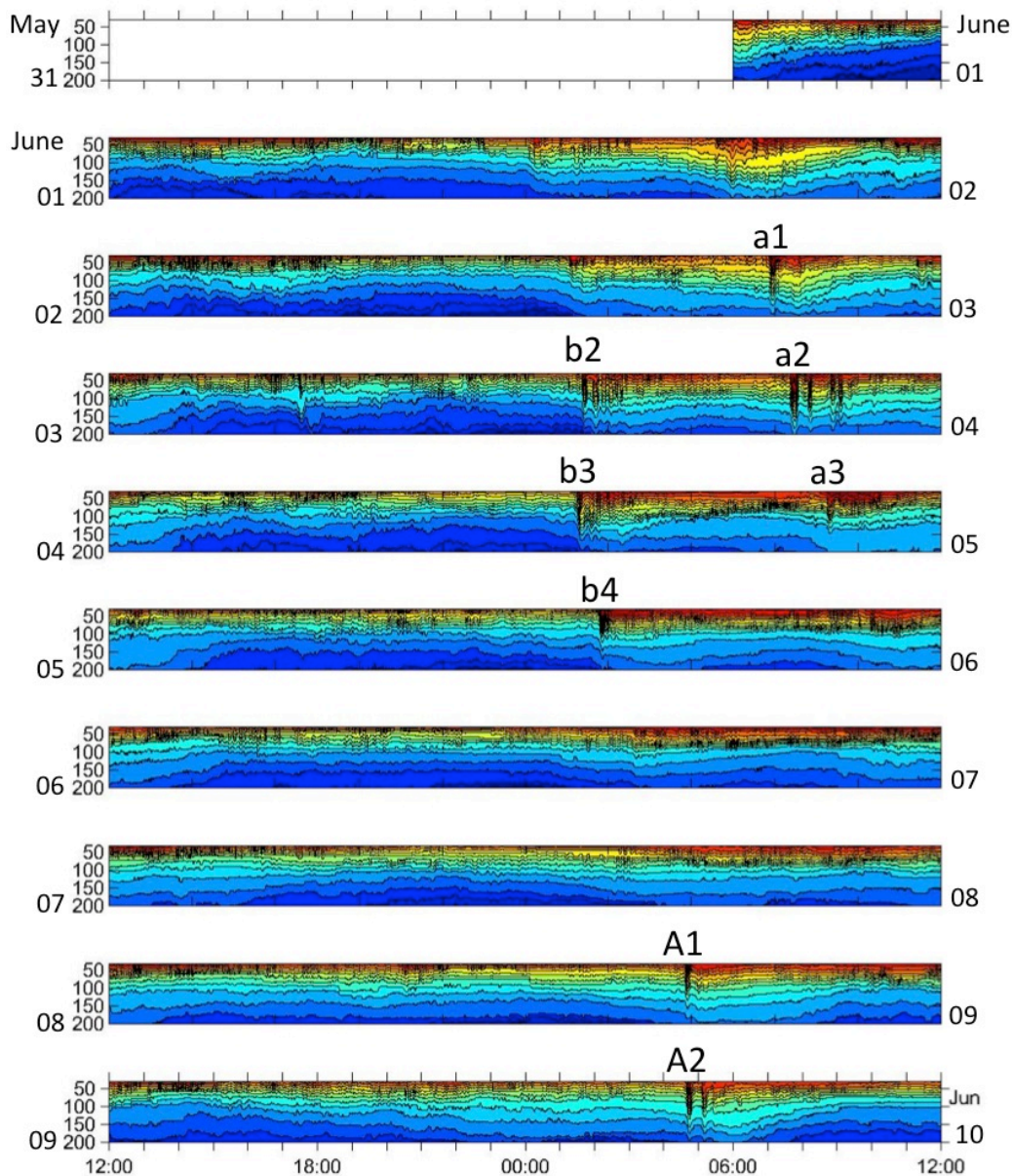


284 always immediately preceded the stronger ebb beat both before and after the
285 switch. This feature is essential to understanding the wave arrival patterns.

286
287 The lagged a- and b-wave arrival times from mooring RPO lined up precisely with
288 the major ebb and flood tidal peaks respectively. (Note that the minor tidal peaks in
289 the Luzon Strait never produced a downstream NLIW at any time.) Each wave
290 arrival has been identified and labeled using a nomenclature which will be
291 maintained throughout the paper. The arrivals were numbered in order of arrival
292 using a lowercase a and b for the first fortnightly “cluster” and an uppercase A and B
293 for the second cluster. Same-pair arrivals received the same number, i.e., B5
294 preceded A5 by about six hours, and so forth. Waves observed during the first
295 cluster were generated after the spring tide when the forcing tidal amplitudes were
296 decreasing. The a-waves were generally stronger however wave b3 was larger than
297 a3. Waves during the second cluster were observed prior to spring tide while the
298 forcing amplitudes were increasing. The A-waves appeared first (A1-A4 had no
299 accompanying B-wave) before the B-waves began arriving on June 10 (B5). The A-
300 waves were generally larger than the accompanying B-wave, except for wave A7 on
301 June 12 which was anomalously weak. Note that 48.6 hours is a mean travel time:
302 larger waves traveled slightly faster due to the contribution from nonlinear wave
303 amplitude. This is why the smaller, slower waves on 6/8 to 6/10 were not lagged
304 quite enough. Altogether the veracity of this pattern-matching exercise is
305 remarkable. The wave arrivals tracked the generating tides quite precisely,
306 regardless of whatever larger-scale oceanographic variability was going on in
307 between.

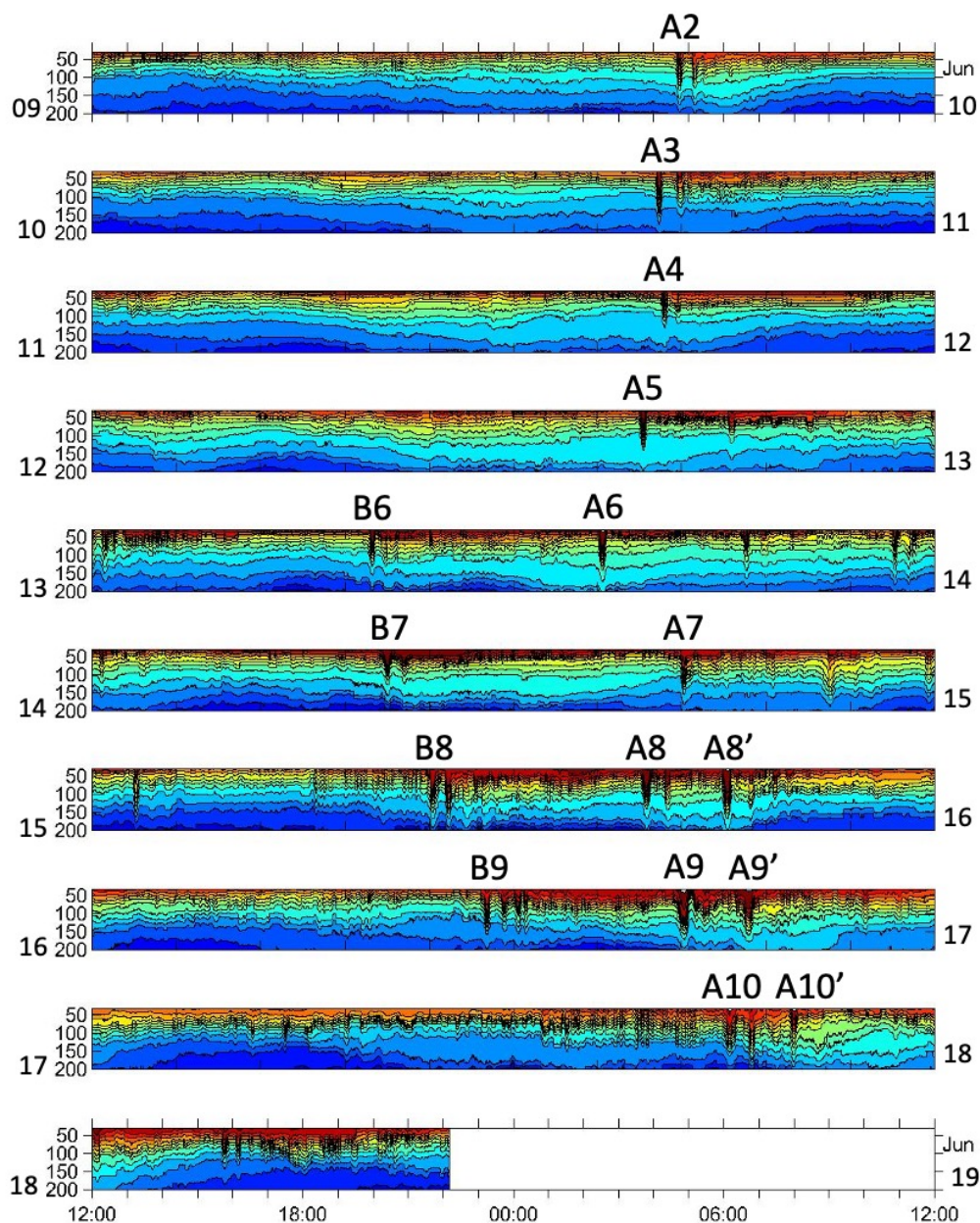
308
309 The timing of the wave arrival patterns over the continental slope can be further
310 illustrated by the daily stack plots of temperature for the entire water column at
311 mooring RPO (Figure 4). These patterns were the same at the other moorings
312 although there were more waves per packet at RPO (see next section). For the first
313 cluster, the a-waves arrived about 30-60 minutes later each day, while the b-waves
314 arrived at about the same time (Figure 4a). Therefore, the arrival time difference
315 between the a- and b-waves was 6-7 hours. This differed from the ASIAEX 2000
316 results nearby, whence the a-waves arrived at nearly the same time each day and
317 the b-waves were delayed each day by about an hour. This difference is attributed
318 to different barotropic tidal forcing in the Luzon Straits during the two experiments.

319
320 For the next cluster, the A-waves arriving on June 9 to 13 arrived at about the same
321 time each day (Figure 4b). From June 14-18, the A-waves arrived about an hour
322 later each day. This result, that the A-wave arrival times were constant early in the
323 fortnightly tidal cycle but delayed an hour per day as the waves increased in
324 amplitude later in the cycle was consistent with the model results of [Chen et al.,
325 2013]. Wave A7 on June 15 was anomalously late by about 2 hours relative to
326 waves A6 and A8. This is attributed to the passing of tropical storm Hagabus on
327 June 14-15 with accompanying strong wind-forced currents. The B-wave arrivals
328 began at about 20:00 on June 13, and were subsequently delayed about an hour per
329 day, similar to the corresponding A-waves (Figure 4b). The difference in the arrival



330
331
332
333
334
335

Figure 4a. Temperature contour plots for mooring RPO from May 31 to June 10, 2014. Each panel from top to bottom is one day centered on midnight, to capture both the a- and b-wave arrivals. The individual waves are labeled to match Figure 3. No waves arrived during June 7-8, corresponding to neap tide in the Luzon Straits.



336
337

338 *Figure 4b. As in Figure 4a, only for the time period June 9 to June 19, 2014. The B-*
339 *wave arrivals began (June 13) five days after the A-waves (June 8). The double A-*
340 *waves (A8'-A10') arrived during June 16-18. Spring tide in the Luzon Straits was on*
341 *June 14, thus the largest waves are expected two days later at the array.*



342
343 times between the B-waves and the A-waves was 6:30, 8:25, 6:15, and 5:50 on June
344 14-17 respectively. Had the June 15 A-wave fit the pattern and not arrived late, the
345 time difference on that day likewise would have been about 6 hours. They could
346 possibly be produced by the same tidal beat at different ridges [Chen et al., 2013]
347 which coincidentally produces timing which is quite similar to the East Ridge ebb
348 tide/flood tide scenario, but the sources may also be separated longitudinally [Ramp
349 et al., 2019]. The fact that wave A7 was delayed by the tropical storm while B7 was
350 not further suggests a different travel path for the two types of waves. Statistically
351 speaking, the directional histograms (not shown) show the A-waves on average
352 traveling along a path about 24 degrees more northward (294°) than the B-waves
353 (270°), indicating that the primary source for the A-waves may be located farther to
354 the south along the Luzon ridge system. Previous authors suggested that there may
355 be two locations for wave generation, one near the Batan Islands and the other near
356 the Babuyan Islands [Du et al., 2008] but they stopped short of relating a certain
357 wave type to a particular source location. Using a three-dimensional moored array
358 and the SUNTANS model, Ramp et al., [2019] attributed the generation of a-waves to
359 the southern Luzon Strait and the b-waves to the north. Lacking observations
360 between YPO2 and the Luzon Strait, we cannot comment further in this paper on the
361 generation problem. While the strong wave arrival/tidal peak correlations suggest
362 once again attributing the a-wave/b-wave generation to the ebb tide/flood tide
363 phenomenon at the East Ridge, there are other possibilities producing similar
364 timing that cannot be ruled out.

365
366 On June 16-18 two A-waves of near equal amplitude arrived about 2 hours apart.
367 These “double A-waves” appeared over the slope only near spring tide in the Luzon
368 Straits, and were also noted in moored observations from farther south near
369 Dongsha [Ramp et al., 2021]. By examining the arrival patterns (Figure 4b) it is
370 apparent that the trailing wave is the “new” one and it has therefore been
371 designated by a prime. The origin of these waves is unclear. They may be formed
372 by a very large wave that “split” well offshore of the Sand Dunes observations. This
373 seems unlikely however since the waves are nearly equal in amplitude, and the
374 second wave may even be larger than the first (see A8 vs. A8' Figure 4b).
375 Alternatively, the new A' wave may originate from a different (third) source in the
376 straits that is only active under maximum barotropic forcing. This would be the
377 internal tide analogy of the famous Maverick's surf break off Half Moon Bay,
378 California, where the surface waves are completely absent until the incoming swell
379 reaches the height required to “feel” the bottom. More observations in the source
380 region are needed to understand this double a-wave phenomenon.

381 382 *3.3 Wave Transformation Over the Slope*

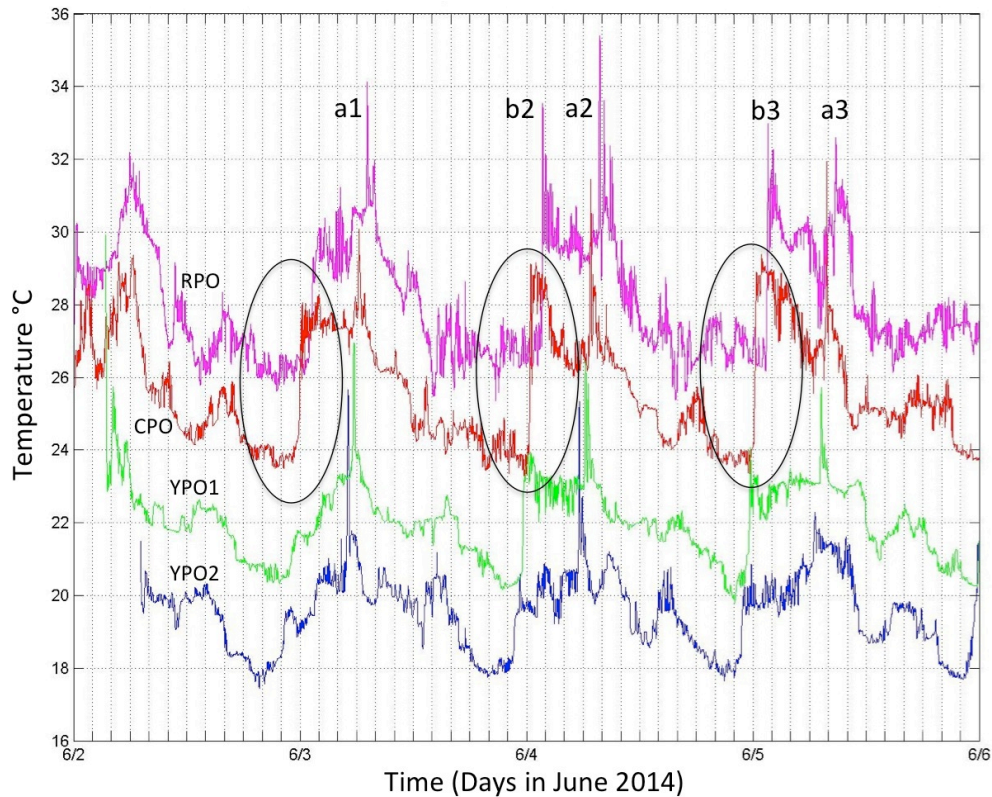
383
384 Many significant wave transformations were observed between the 386 m (YPO2)
385 and the 266 m (RPO) isobaths over the upper continental slope. Three sections of
386 the record are shown to illustrate different phenomena. The first sequence from
387 June 2 to 6 evolved out of moderate and decreasing forcing in the Luzon Strait



388 (reference Figure 3). The observations captured the local steepening and breaking
389 of the tidal front to form b-waves as it shoaled (Figure 5). The internal tides at YPO2
390 were diurnal and nearly sinusoidal with an amplitude of about 4°C (blue line). The
391 a-waves were already evident at YPO2, but not the b-waves. Then, beginning at
392 YPO1 and continuing to CPO, the leading edge of the tidal front became very steep
393 with a temperature change of 1°C / min for 5 minutes at CPO (black ellipses in
394 Figure 5). This front subsequently broke and formed b-wave packets b2 and b3
395 observed at mooring RPO. This example thus demonstrates a local b-wave
396 formation process via steepening of the leading edge of the tidal front. We show
397 subsequently that this steepening temperature front was due to velocity
398 convergence at the head of the westward-propagating internal tide. The formation
399 of a similar bore-like feature at shallower depths (200 m – 120 m) was noted in the
400 ASIAEX data [Duda et al., 2004] but they did not make the connection to b-wave
401 formation. Waves a1 and a2 lost amplitude and formed packets as they shoaled
402 between YPO2 and RPO. This process will be compared with some recent
403 theoretical ideas in the discussion section. Wave a3 was small at YPO2 but gained
404 amplitude as the tide progressed up the slope. This is because the barotropic
405 forcing in the Luzon Strait was weaker on June 5 than on June 2-4 (ref. Figure 3). All
406 the waves subsequently disappeared on June 7-8 during neap tide in the Luzon
407 Strait.

408
409 The second sequence during June 10-14 shows well developed A-wave packets
410 which originated from moderate but increasing remote forcing (Figure 6). Only A-
411 waves were observed until June 13 when the B-waves started to arrive. Wave B6
412 was weakly perceptible at YPO2 and increased in amplitude across the slope. The
413 temperature fluctuations induced by the A-waves increased across the slope and
414 reached a maximum of 7°C on June 11 at A3. The temperature gradients in the wave
415 fronts were again very steep, 1°C / min. The number of waves per packet increased
416 towards shallower water, most clearly in waves A2, A3, and A4. Two extraneous
417 solitary waves appeared trailing wave A5 on June 13 at CPO and RPO but were not
418 part of the A5 packet structure. Two similar waves appeared the next day (Figure 7)
419 and their origin is unclear.

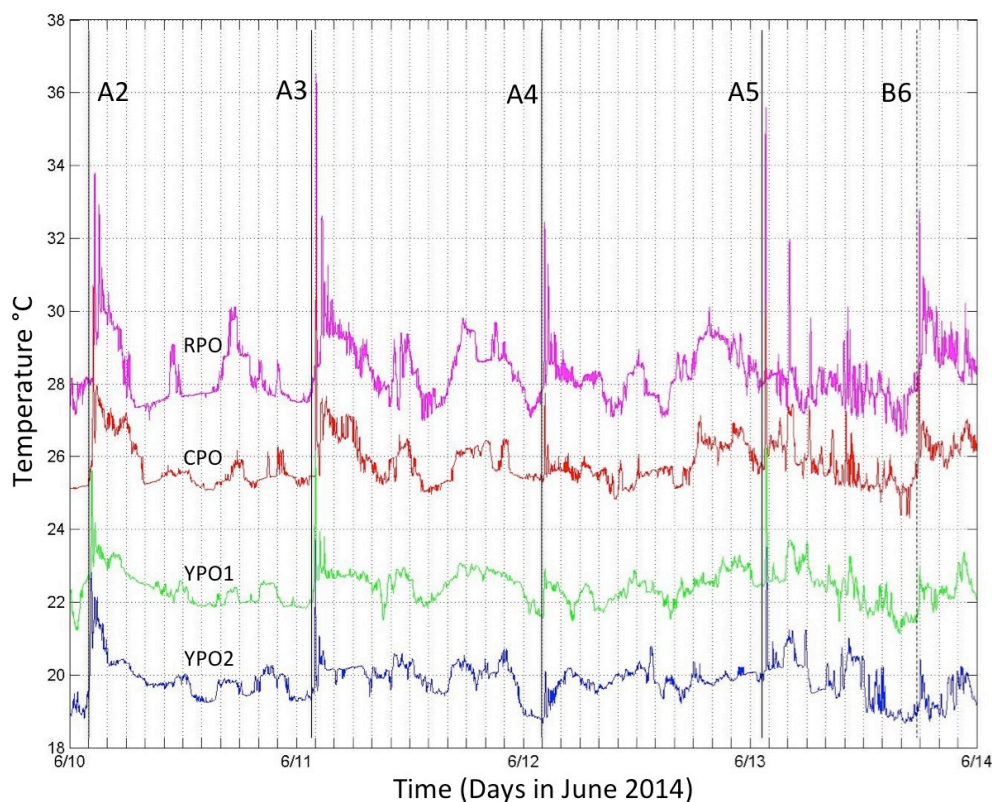
420
421 The final sequence from June 14 to 18 was obtained during a period of maximal
422 forcing near spring tide at the source, and a very complicated field of NLIW emerged
423 (Figure 7). The B-waves were large and were evident at all the moorings. Wave B8
424 and B9 were solitary at YPO2 but had many waves per packet by the time they
425 reached RPO. The arrival timing was the same as the locally formed b-waves
426 (Figure 5) suggesting similar dynamics but faster/shorter development
427 time/distance when the forcing at the source was stronger. The A-waves continued
428 to grow at YPO2 during June 14-18. Interestingly, the temperature fluctuations due
429 to the largest waves did not increase monotonically as they traveled up the slope
430 from YPO2 to RPO. This is more clearly seen in a bar graph showing the maximum
431 amplitude of the isotherm of maximum displacement (Figure 8). Smaller waves
432 (June 9-12) gained amplitude as they shoaled. All waves larger than about 50 m



433
434
435
436
437
438
439
440
441
442
443
444
445
446
447
448
449
450
451
452
453
454

Figure 5. Temperature vs. time during June 2-6 at all four moorings across the continental slope. The observations are from 75m, 79m, 97m, and 99m from moorings RPO, CPO, YPO1, and YPO2 respectively. Each time series has been offset vertically by 2 °C for clarity. The black ellipses highlight the region of strong temperature fronts at CPO that subsequently broke and formed b-waves at RPO.

offshore (June 13-18) lost amplitude as they shoaled, most clearly between CPO and RPO, where the biggest change in bottom depth and slope occurred. This result is consistent with the numerical results of [Lamb and Warn-Varnas, 2015] who also found that smaller amplitude waves continued to gain amplitude into shallower water but the larger waves did not. This fundamental result, that NLIW first gain amplitude and then lose it as they shoal, is consistent with EKdV theory [Small, 2001; Vlasenko et al., 2005]. Note that all the wave amplitudes (Figure 8) are much less than those observed in the ASIAEX and WISE/VANS region located 43.7 km along the topography towards the southwest. This is because, as seen in hundreds of satellite images (typified by Figure 9), the NLIWs have maximum amplitude in the region just north of the Dongsha Plateau near 20°N decreasing both northward and southward from there. The Sand Dunes site is actually near the northeastern



455
456

457 *Figure 6. As in Figure 5, except during June 10-14, 2014. In this plot, the time series*
458 *have additionally been shifted relative to YPO2 by the propagation time between*
459 *moorings so that individual waves line up. The lag times used are 36.5 min for YPO1,*
460 *66.8 min for CPO, and 122.8 min for RPO.*

461

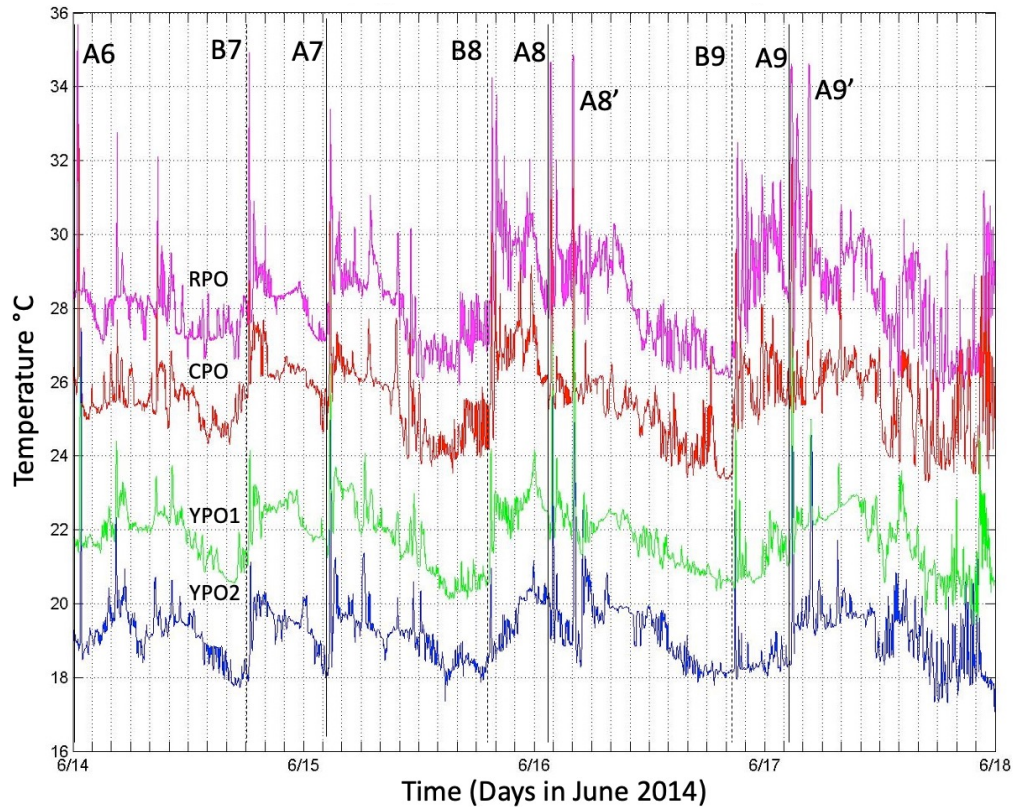
462 extremity of the wave crests as viewed in the imagery: a bit farther to the northeast
463 the waves vanished.

464

465 The double A-wave phenomenon mentioned earlier (Figure 4b) was again evident in
466 Figure 7. These waves differed from the smaller waves trailing A5 and A6 in that
467 they were already well-developed by the time they arrived at YPO2. As in Figure 6,
468 many waves which were solitary at YPO2 formed packets as they crossed the array.
469 Waves B9, A9, and A9' can be clearly seen in the satellite ocean color imagery
470 (Figure 9). The timing of the imagery at 0310 is conveniently just as wave A9 was
471 impacting mooring YPO2. The B-wave packets and solitary nature of A9 and A9' are
472 easily seen in the image.

473

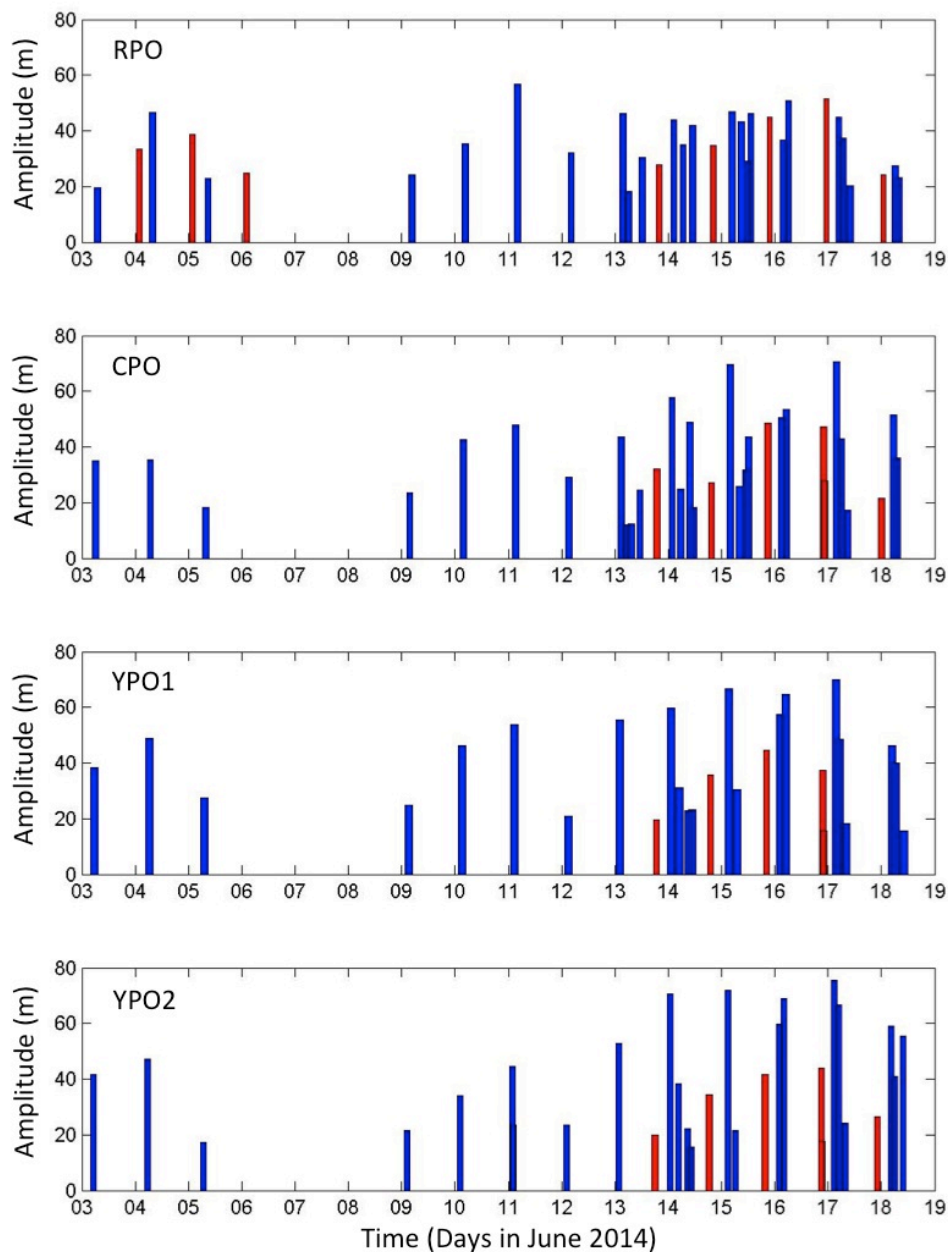
474 Two examples of velocity and temperature across the slope are shown to illustrate
475 the difference between weakly and strongly forced waves. Mooring YPO1 is not
476 shown since it was very similar to mooring YPO2. The weaker case begins at YPO2



477
478
479
480
481

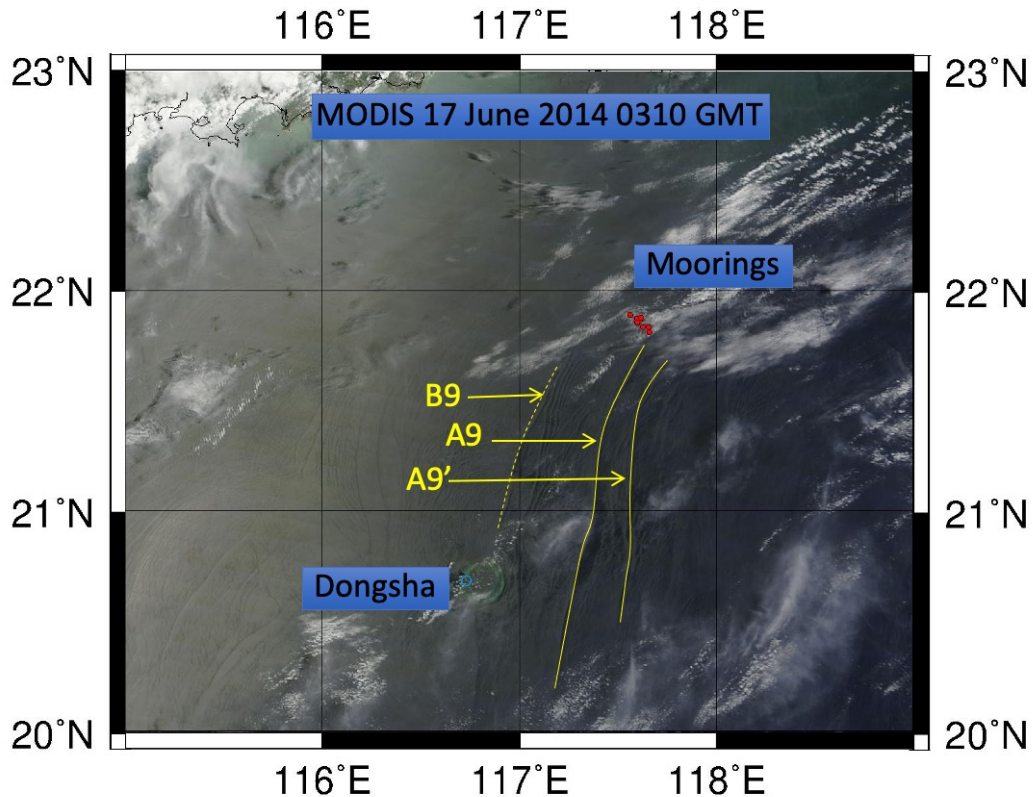
Figure 7. As in Figure 6 except for June 14-18.

482 on June 3-4 (Figure 10, column 1) which shows a clear a-wave near 0530 but no b-
483 wave. Wave a2 was observed towards the rear of the northwestward-propagating
484 internal tide (blue near the surface). The a-wave was traveling NW near the surface
485 and in the opposite direction in the lower water column, with a nodal point near 100
486 m. While not obvious in temperature, the velocity plots show a weak second wave
487 about 20 min behind the lead wave forming a 2-wave packet. By mooring CPO
488 (column 2), located 7.3 km away, the leading edge of the internal tide had steepened
489 to form a sharp front in both velocity and temperature near midnight on June 3.
490 There was strong convergence in the upper 50 m with eastward flow (yellow) ahead
491 of the front and westward flow (blue) behind it. A solitary b-wave appeared on this
492 convergent front which was absent at YPO2. Wave a2 at CPO looked similar to
493 YPO2, perhaps slightly stronger. By mooring RPO, 5.7 km and 80 m farther up the
494 slope (column 3), the b-wave increased in amplitude and formed a 2-wave packet,
495 and the leading a-wave spawned a 4-wave packet. These waves were particularly
496 clear in the v -component since the waves refracted towards the north as they
497 propagated up the slope (Figure 1). The nodal point remained near 100 m for all the



498
499
500
501
502
503
504

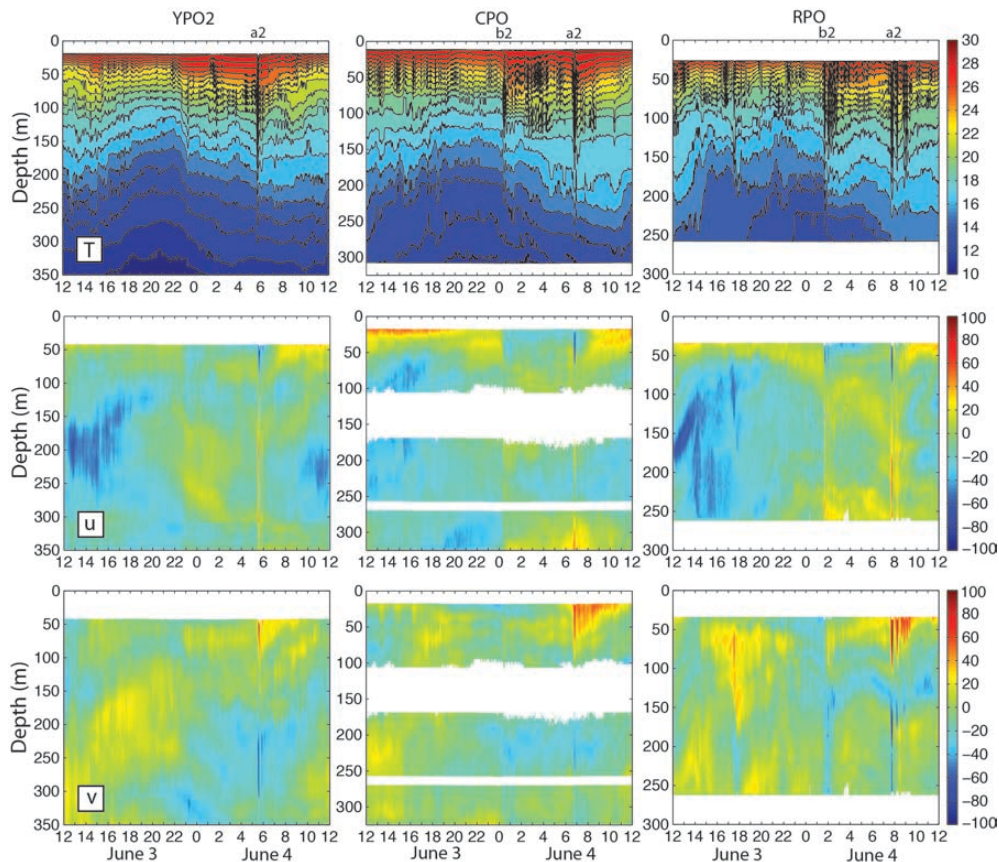
Figure 8. Bar graph of wave amplitudes across the slope. The amplitudes were calculated as deviations of the 20 °C isotherm from its mean position. The a-waves are indicated by blue bars and the b-waves by the red.



505
506
507
508
509
510
511
512
513
514
515
516
517
518
519
520
521
522
523
524
525

Figure 9. A sea surface ocean color image obtained at 0310 on June 17, 2014 from the Moderate Resolution Imaging Spectroradiometer (MODIS). The Sand Dunes moorings are indicated by the red dots. The site of the former ASIAEX and WISE/VANS mooring S7 is indicated by the yellow triangle. The surface signatures of NLIWs B9, A9, and A9' are indicated by the yellow arrows. Wave A9 was impinging upon mooring YPO2 at this moment, as seen in Figure 7.

leading waves. Note that the background internal tide (most easily seen in the deep water) was diurnal at moorings YPO2 and CPO but became more semidiurnal at RPO. This indicates the presence of a locally generated tide at RPO where the bottom slope was steeper than at the other moorings farther offshore. In fact, the bottom slope at YPO2-CPO (Figures 1, 2 right of the dotted white line) was critical to the diurnal tide while the slope at RPO (left of the dotted white line) was critical to the semidiurnal tide. The interaction of the tidal currents with the bottom is maximal where the slope of the tidal beams parallels the bottom and this likely contributes to the different nature of the sand dunes offshore vs. onshore of the dotted white line (Figure 2). This point is taken up further in a subsequent work.



526
527

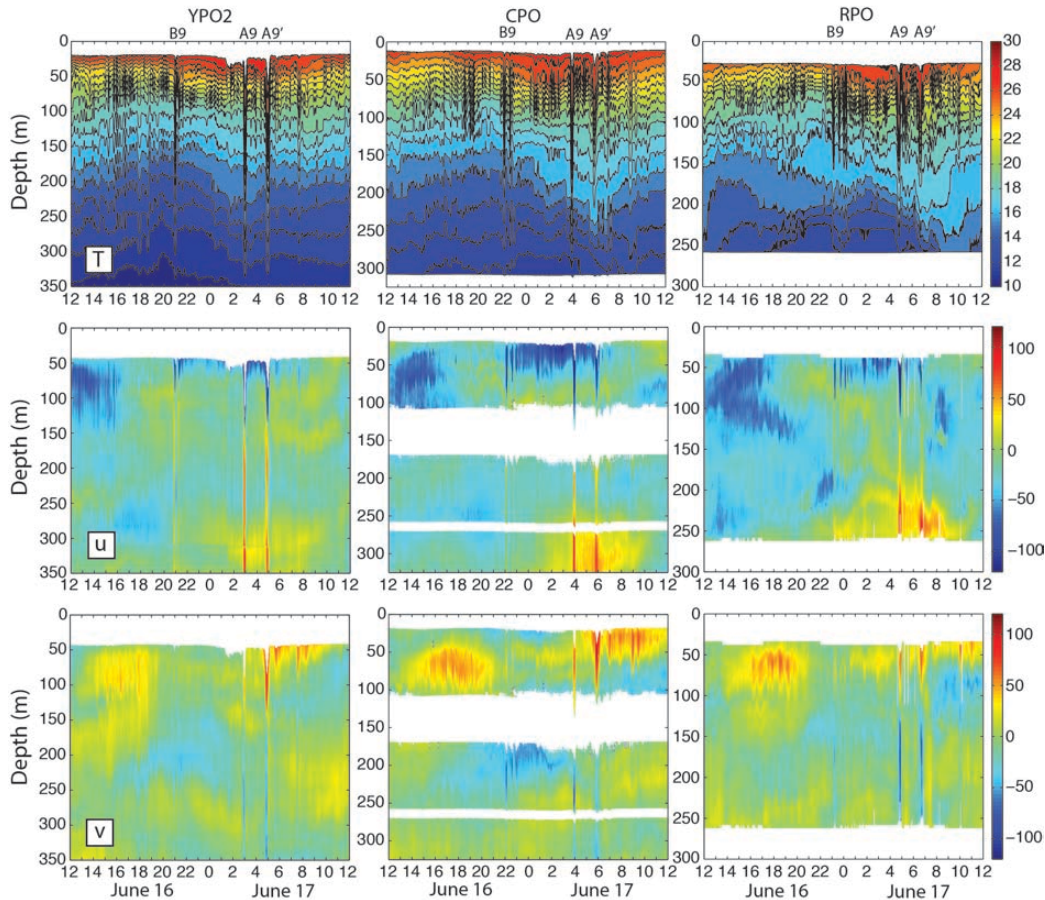
528 *Figure 10. Temperature (top), u-component of velocity (middle) and v-component of*
529 *velocity (bottom) from 3-4 June 2014 from moorings YPO2 (left), CPO (center), and*
530 *RPO (right). The wave propagation time between moorings was 67 min from YPO2 to*
531 *CPO, and 56 min from CPO to RPO. Positive (u, v) represents (east, north) respectively.*
532 *White space at mooring CPO indicates regions not sampled by the three ADCPs. These*
533 *data were obtained during a period of moderate and declining tidal forcing, see*
534 *Figures 3 and 5 for context.*

535

536 At all moorings, there was only one westward surface internal tide per day. The b-
537 waves all emerged at the leading edge of this westward tide, while the a-waves
538 emerged towards the rear, and this clear velocity signature represents another way
539 to distinguish the two types of waves. The two wave arrivals were separated by
540 6:20 on this day. The strongest bottom velocities were down-slope (southeast) and
541 were greater in the NLIW than in the internal tide.

542

543 The strong example (Figure 11) shows that unlike the previous example, both the B-
544 wave packet and the A-wave packet had already formed by mooring YPO2 on June
545 16-17. (Remember there is no dynamical significance to upper vs. lower case a, b:



546
 547
 548
 549
 550
 551
 552
 553
 554
 555
 556
 557
 558
 559
 560
 561
 562
 563

Figure 11. As in Figure 10, except for June 16-17, 2014. These data were obtained during a period of strong tidal forcing, see Figures 3 and 7 for context.

the lettering is chosen to remain consistent with the nomenclature established in the earlier figures and refers to the first and second cluster.) The waves were traveling in the same direction as the June 3-4 waves, but had a deeper nodal point located near 120-130 m. The A-wave in this case was a double A-wave mentioned earlier. These resembled individual waves rather than a packet in the usual sense. The two waves A9 and A9' were about the same amplitude: on this day the first wave (A9) was slightly larger but the opposite was true the day before (not shown). The A9' wave was slightly wider than the A9 wave. This may be due to constructive interference with the tail of wave A9 which was just two hours ahead of it. Wave B9 formed a 2-wave packet at CPO (column 2) and a 3-wave packet at RPO (column 3). Wave A9 formed a 2-wave packet between moorings CPO and RPO. As before, the u-component shows the B-wave was coming off the leading edge of the westward



564 surface tide (eastward bottom tide). The A9 wave grew out of the middle of the tide
565 and the A9' wave emerged from the trailing edge of the same westward internal
566 tide. The surface westward velocities exceeded 97 cm s^{-1} , 162 cm s^{-1} , and 153 cm s^{-1}
567 at YPO2, CPO, and RPO respectively. The eastward bottom velocities exceeded 20
568 cm s^{-1} , 85 cm s^{-1} , and 80 cm s^{-1} respectively. The smaller lower layer velocities
569 below the nodal point were consistent with a thicker lower layer and with theory
570 [Lamb and Warn-Varnas, 2015]. The strongest bottom velocities outside the waves
571 were about half the wave velocities. Clearly the strongest bottom velocities
572 observed over the upper continental slope were generated by the passing NLIWs,
573 although these high velocities were very brief compared to the internal tide.
574 Referring once again to Figure 8, the B-wave (just before midnight on June 16)
575 started at YPO2 with just over 40 m amplitude and grew shoreward across the shelf.
576 In contrast, the much larger A-waves just after midnight on the 17th started out
577 with 70 – 75 m amplitude at YPO2 and lost amplitude across the shelf. This is
578 consistent with the earlier discussion surrounding Figure 10.

579
580 Many ordinary internal waves can be seen in Figure 11 in between the nonlinear
581 waves. These waves were likely generated by tropical cyclone Hagabus which
582 passed over the array on June 14-15 with winds exceeding 25 m s^{-1} .

583
584 On June 16 a packet of convex mode-2 waves appeared from 1500-2100 centered
585 near 60 m and extending from 50 to 100 m depth (Figure 11, bottom row). These
586 waves strengthened upslope from YPO2 to RPO and trailed the double-A waves
587 from the day before (not shown). There looked to be about 6 waves in the mode-2
588 packet at mooring RPO. All three of the double-A waves on 16, 17, and 18 June had
589 this feature associated with them. The observation is consistent with [Yang et al.,
590 2009, 2010] who observed mode-2 waves trailing mode-1 waves in the ASIAEX
591 region nearby and attributed this to the adjustment of shoaling mode-1 waves.
592 These observed wave transformations are now discussed further below in light of
593 the published theory for shoaling solitary waves.

594 595 **4 Discussion**

596 597 *4.1 The physics of shoaling waves*

598
599 The response of shoaling NLIWs over a sloping bottom depends critically on three
600 factors: the bottom slope, wave amplitude, and thermocline depth [Small, 2001;
601 Vlasenko and Hutter, 2002; Lamb, 2002; Vlasenko and Stashchuk, 2007; Grimshaw
602 et al., 2014; Lamb and Warn-Varnas, 2015]. Over very slight slopes, waves shoal
603 adiabatically with little change in form. The wave amplitudes first increase
604 gradually and then rapidly decrease, with the depth of maximum amplitude
605 depending on the details of the wave's initial amplitude, stratification, and bottom
606 slope [Lamb and Warn-Varnas, 2015]. For the ASIAEX region nearby, they found the
607 depth of maximum amplitude to be between 400-300 m. The width of the wave is
608 inversely proportional to the amplitude, so the waves become wider once the
609 amplitude starts to decrease.



610
611 As the bottom steepens, or alternatively the wave amplitude increases, a shoaling
612 solitary wave tends to form packets via the formation of a trailing dispersive tail.
613 When the bottom is steeper still, the combination of bottom slope, wave amplitude,
614 and fractional upper layer thickness (set by the bottom depth and undisturbed
615 thermocline depth) determine the onset of wave breaking and/or reflection. These
616 concepts can be quantified: using a fully nonlinear two-dimensional model with
617 continuous stratification, Vlasenko and Hutter [2002] studied shoaling solitary
618 waves using bottom topography and stratification appropriate for the Andaman and
619 Sulu Seas. As the wave shoals, the trough slows down relative to the surface, which
620 causes the leading edge of the wave to flatten out and the back of the wave to
621 steepen. The wave effectively breaks (from the back) when the orbital velocity (u)
622 exceeds the propagation speed (C_p). This concept has also been observed in the
623 field [Lien et al., 2012; 2014]. By means of multiple model runs varying the bottom
624 slope and non-dimensional wave amplitude, [Vlasenko and Hutter, 2002]
625 established a generalized criteria to determine the wave parameter space for which
626 breaking or dispersion will occur (their Figure 8). The criteria is that:
627

$$628 \quad \bar{a} = \frac{a_m}{H_b - H_m} = \frac{0.8^\circ}{\gamma} + 0.4 \quad (1)$$

629
630 where \bar{a} is the non-dimensional wave amplitude, a_m is the wave amplitude, H_b is the
631 local bottom depth, H_m is the undisturbed thermocline depth, and γ is the bottom
632 slope given in degrees. Note that this expression does not depend on the details of
633 the stratification, which were examined using the model and made little difference
634 to the results. If the slope and thermocline depth are known, this expression can be
635 used to evaluate the isobath where a wave of given amplitude will break, or
636 alternatively, to determine what wave amplitude would be required for a wave to
637 break at a given isobath.
638

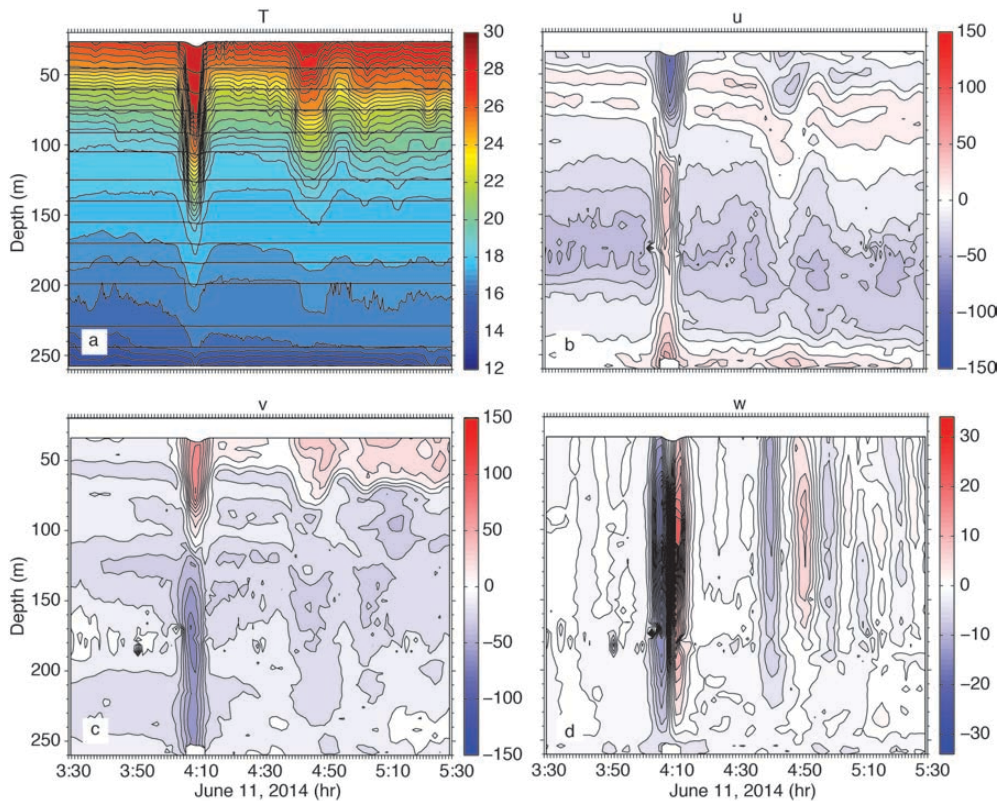
639 For the Sand Dunes data set, these criteria are examined for moorings CPO and RPO.
640 Mooring CPO, at 342 m depth, was located on a very shallow slope ($.006 = 0.3^\circ$)
641 among the largest sand dunes (Figure 2) while mooring RPO, at 266 m depth, was
642 located on a steeper, but still fairly shallow slope ($.03 = 2^\circ$) among the smaller dunes
643 with shorter wavelengths. The isotherm of maximum displacement was 23°C at
644 both mooring locations. The undisturbed isotherm depth, determined by time-
645 averaging the low-pass filtered data, was similar at both moorings, 60 m at CPO and
646 57 m at RPO. Substituting these values in (1) shows that a wave amplitude of 846m
647 would be required at CPO for wave breaking at this location. This extremely large
648 value results from both the gentle bottom slope and the shallow thermocline ($H_b -$
649 $H_m = 282$ m). Clearly no wave breaking events are expected at site CPO. Moving on
650 to RPO, the required amplitude for wave breaking there would be only 167 m.
651 Waves this large have been commonly observed farther to the southeast near site S7
652 and Dongsha Island, however wave amplitudes at the Sand Dunes site never
653 exceeded about 80 m at YPO2 and 60 m at RPO (Figure 8). Therefore, according to



654 (1) both sites fall on the “dispersion” side of the Vlasenko and Hutter [2002] curve
655 (their Figure 8), and we do not expect wave breaking to occur anywhere in the Sand
656 Dunes array. Note waves may also break due to shear instability across the nodal
657 point if the Richardson number falls below 0.25. This usually only happens for flat-
658 bottom waves in shallow water [Lamb, 2002], a condition which was never
659 approached in the Sand Dunes array area.

660
661 In spite of this negative expectation, individual waves were examined in detail for
662 evidence of trapped cores, wave asymmetry, or anything else that would indicate
663 wave breaking. The arguments above suggest that if wave breaking were to
664 manifest itself, it would most likely be at site RPO where the bottom is steeper, the
665 orbital velocities stronger, and the phase speed slower than at the other three sites.
666 The temperature and velocity structure at site RPO are therefore shown for three
667 examples: a statistically common a-wave (Figure 12), a very large a-wave (Figure
668 13) and a b-wave (Figure 14). For wave A3 on June 11 (Figure 12), which typifies A-
669 waves between June 3-13, the wave was symmetric in both velocity and
670 temperature with no sign of back-side steepening. The wave amplitude was 57 m
671 and the maximum orbital velocity was 104 cm s^{-1} and was located near the surface.
672 The opposing lower layer velocity was order 75 cm s^{-1} commensurate with the
673 thicker lower layer. The w-profile was nearly symmetric at $\pm 25 \text{ cm s}^{-1}$, downward
674 ahead of the wave and upward behind it, with the maxima located near mid-depth.
675 One or possibly two trailing waves were observed: the first was centered near 4:48
676 and had vertical velocities of $\pm 8 \text{ cm s}^{-1}$ while the second was near 5:00 with vertical
677 velocities of just a few cm s^{-1} . A fourth wave-like feature was observed in the
678 temperature plot near 5:20 but it cannot be discerned in the velocity structure. To
679 summarize, wave A3 consisted of a primary wave and 2-3 trailing waves about 30
680 min behind. The velocity structure had open contours all the way up the minimum
681 depth of the observations, with a maximum of 104 cm s^{-1} which is \ll the local
682 propagation speed of 1.69 cm s^{-1} . The wave was symmetric in velocity and
683 temperature with no sign of a trapped core.

684
685 The largest wave observed was wave A9 on June 17. This wave showed several
686 characteristics of breaking or near-breaking waves (Figure 13). The back side of the
687 wave was steeper than the leading side, and the jagged temperature contours in the
688 wave core were indicative of breaking and/or mixing. A “pedestal” was starting to
689 form behind the wave as described by [Lamb and Warn-Varnas, 2015]. Several
690 more smaller depression waves were emerging from the “pedestal.” The velocity
691 contours were likewise asymmetric and showed a subsurface maximum near 60-70
692 m which was about 20 cm s^{-1} greater than the surface. This is typical of waves with
693 trapped cores [Lien et al, 2012, 2014; Lamb and Warn-Varnas, 2015]. The
694 maximum near-surface velocity was 155 cm s^{-1} , which was close to the local phase
695 speed. It is possible that the surface velocities above 20 m depth were slightly
696 larger but were not observed. At site CPO, this same wave had a maximum velocity
697 of 180 cm s^{-1} , also very close to the local phase speed. The vertical velocities were
698 actually smaller than wave A3, at -12 and $+20 \text{ cm s}^{-1}$ with at least two and possibly
699 more of the trailing depression waves visible as down/up pairs. To summarize, this



700
701
702

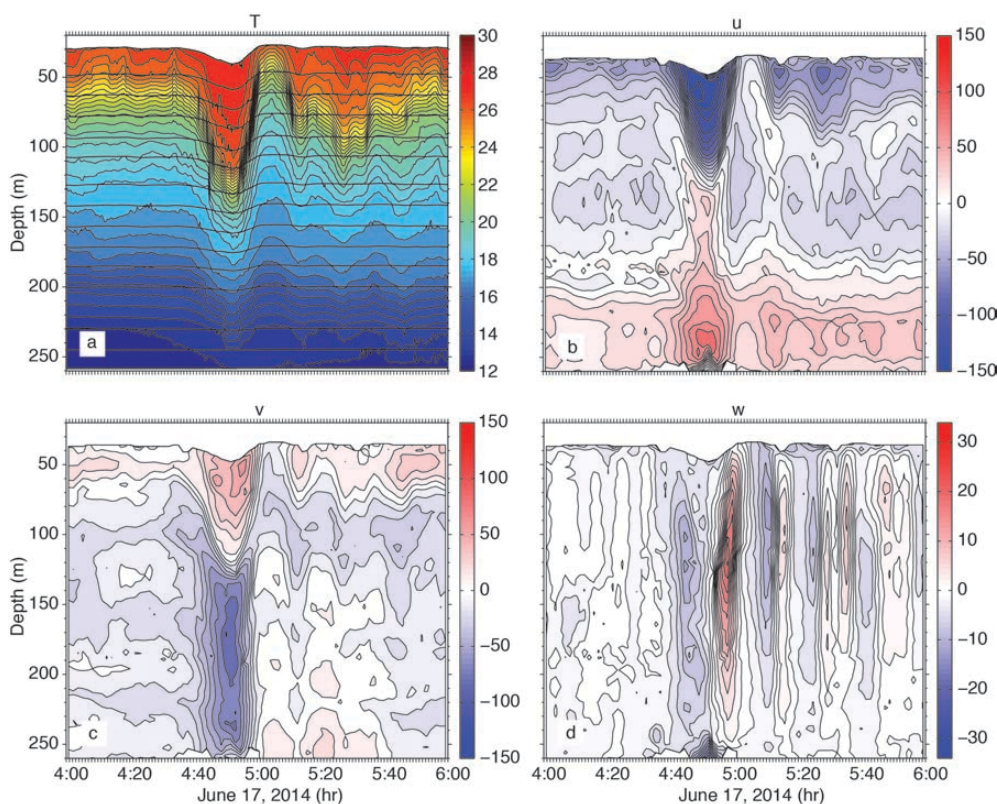
703 *Figure 12. a) temperature, b) u-component of velocity (positive east), c) v-component*
704 *of velocity (positive north), and vertical velocity (positive up) for wave A3 on June 11,*
705 *2014. This rank-ordered packed with a symmetrical leading wave typifies most of the*
706 *type-a waves observed during the experiment.*

707

708 wave appears to be about to break or just starting to break, however, this wave was
709 the exception rather than the rule: only one such wave was observed. It is possible
710 that the trailing double-A waves A8' and A9' might also meet these criteria, however
711 their form was distorted by interference from the trailing packet of the leading A8
712 and A9 waves two hours earlier, making their characteristics difficult to discern.

713

714 It is worth noting that subsurface maxima in the wave may be caused by phenomena
715 other than wave breaking. Tropical cyclone Hagabus passed over the array on June
716 14-15 and forced strong near-surface currents which opposed the wave velocities.
717 This was especially obvious on June 15 (not shown) when westward currents at 80
718 m depth in wave A7 exceeded the surface currents by over 80 cm s^{-1} at RPO and by
719 over 100 cm s^{-1} at CPO. This likely explains why wave A7 arrived 2 hours late with
720 respect to waves A6 and A8 (Figure 4b). The storm also left behind a surface mixed
721 layer 40 m deep which lingered to the end of the record. This means all the largest

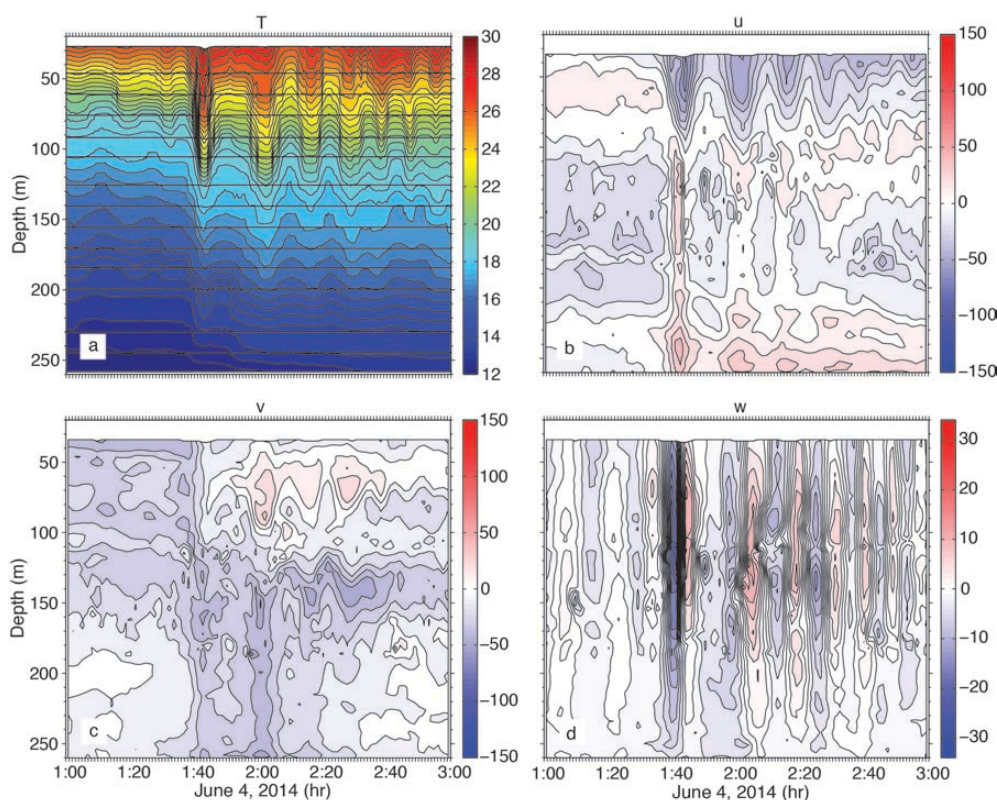


722
723
724
725
726
727
728
729
730
731
732
733
734
735
736
737

Figure 13. As in Figure 12, but for wave A9 on June 17, 2014. The steepening back side and subsurface velocity maximum suggest breaking or imminent breaking.

waves forced near spring tide propagated into a region with an unusually deep surface mixed layer. The effect of this is to severely limit wave breaking [Lamb, 2002]. In fact, the scenario described above in the results section rather closely resembles the model results of [Lamb, 2002] when a surface mixed layer was added (their Figure 10). The shoaling solitary wave in the model produced a second trailing solitary wave, followed by the dispersive tail of mode-1 depression waves, followed by a packet of mode-2 waves. The observations reported here closely resembled this pattern not only on June 16-18, but also on June 3-5 trailing waves a1 and a2.

738 We conclude that most of the packets that formed as the waves traveled up the
739 slope from YPO2 to RPO were formed by dispersion rather than wave breaking.
740 Rotational effects seem locally unimportant, given that the packets formed in just
741 two hours while the local inertial period was 32 hours. Rotation may have played a
742 role farther offshore, establishing the initial perturbations (inertial gravity waves)
743 that then grow and become a trailing packet as the waves shoal [Grimshaw et al.,



744

745 *Figure 14. As in Figure 12, except for wave b2 on June 4, 2014. This example typifies*
746 *waves formed locally by breaking of the tidal front between moorings YPO and RPO.*
747

748

2014]. We are not able to investigate this effect without observations in deep water.
749 Trailing undular bores of the sort modeled by [Grimshaw et al., 2014] by including
750 rotation were not observed, but are likely not observable since in the real ocean, the
751 waves arrive periodically and the trailing undular bores would be destroyed by each
752 subsequent arriving NLIW before they have a chance to develop. It is most likely
753 then an imbalance between nonlinearity and dispersion that causes the new trailing
754 waves to form [Vlasenko and Hutter, 2002; Lamb and Warn-Varnas, 2015]. The
755 large lead ISW in the Sand Dunes array never split in two, but rather slowly
756 decreased in amplitude as energy was transferred to the dispersive tail. Phenomena
757 such as wave splitting and breaking likely took place inshore of the sand dunes
758 array in the vicinity of the 150 m isobath, as was observed previously at the ASIAEX
759 site nearby.

760

761 The situation for the locally formed b-waves (b2-b4) was completely different.
762 These waves were non-existent at YPO2 but formed well-defined, evenly spaced
763 packets by the time they reached RPO (Figure 14). For wave b2 on June 4, six waves



764 can be clearly seen in T and w, with most all the horizontal velocity in u, that is these
765 waves were traveling westward. The amplitude of the lead wave was about 40 m,
766 the near surface velocity 60 cm s^{-1} westward, and near-bottom velocity 40 cm s^{-1}
767 eastward. The waves were formed all at once by the collision and breaking of the
768 westward internal tide with the off-slope propagating eastward tide. This is a
769 different mechanism than that described for shoaling ISWs in the literature.

771 *4.2 Energy and energy flux*

772
773 The data set provides an opportunity to observe how the horizontal kinetic (HKE)
774 and available potential (APE) energy in the high-frequency nonlinear internal waves
775 changes as the waves propagate up a gentle slope. In turn, the energy pathways
776 provide some insight to the dynamics underlying the wave transformation process.
777 The theoretical expectation for linear and small-amplitude nonlinear internal waves
778 is that the energy will be equipartitioned for freely propagating long waves away
779 from boundaries. This is not the case however for finite amplitude nonlinear,
780 nonhydrostatic internal solitary waves whose KE typically exceeds the PE by a factor
781 of 1.3. This result was found theoretically via exact solutions to the fully nonlinear
782 equations of motion [Turkington et al., 1991] and has also been noted
783 observationally [Klymak et al., 2006; Moum et al., 2007]. Thus, the KE is expected to
784 slightly exceed the PE for the waves arriving at mooring YPO2. For shoaling NLIW
785 however, the flux of PE greatly exceeds the flux of KE which causes the PE to exceed
786 the KE in shallower water [Lamb, 2002; Lamb and Nguyen, 2009]. This is because
787 the flux of PE remains nearly constant while the KE flux decreases as the upper and
788 lower layer thicknesses become more equal. Shoaling waves observed in the
789 Massachusetts Bay displayed this property [Scotti et al., 2006]. Thus, a shift from
790 greater KE to greater PE might be expected as the waves shoal from YPO2 to RPO,
791 although it depends on the details of the wave amplitude, stratification, bottom
792 slope, etc.

793
794 To compute the energies and energy fluxes from moorings, time series of density
795 and velocity which are uniform in space and time are required. Moorings RPO and
796 CPO had good coverage of temperature and salinity in the vertical (Table 1)
797 however moorings YPO1 and YPO2 sampled temperature only. Two methods to
798 compute the density at YPO1 and YPO2 were explored. The first used a constant
799 salinity (34.42, the vertical average from a nearby CTD cast) paired with the
800 observed temperature at each sensor to compute density. This method assumes
801 that most of the density variability comes from the temperature fluctuations rather
802 than salinity. The second method used the salinity profiles from all the CTD casts
803 taken during the cruise to compute a mean T/S curve, which was then used as a
804 look-up table to determine the salinity to use with each observed temperature. The
805 CTD casts were all within 12 km of each other and were thus treated as a time
806 series. The profiles fell into two groups, namely before tropical storm Hagabub
807 passed by on June 14, with little-to-no surface mixed layer, and after the storm when
808 the mixed layer was about 40-50 m deep. Thus, two mean T/S curves were actually
809 used, one from before the storm and one after. The benchmark for these methods



810 was to compare the density calculated using the T/S curves with the actual density
811 calculated using the observed salinity on moorings RPO and CPO. The APE
812 computed using the mean T/S curve was found to agree much better with the
813 observations than the APE computed using a constant value for the salinity. Both
814 techniques were slight underestimates of the true APE, but the T/S method much
815 less so than the constant method. For this reason, the mean T/S curves were used
816 to compute the density time series, and thus APE for moorings YPO1 and YPO2.

817
818 The observed time series also had velocity gaps of varying severity in the water
819 column due to the range limitations of the ADCPs. Mooring CPO had a mid-depth
820 gap spanning roughly 110-170m and a second smaller gap from 255-265m (see
821 Figures 10 and 11). These gaps were filled using the least squares fit normal mode
822 techniques described in [Nash et al., 2005]. Theoretically as many as seven modes
823 (number of instruments in the vertical – 1) were possible, but the most stable
824 results were achieved with just three modes. No attempt was made to fill in the
825 upper 20 m of the water column where both velocity and temperature were
826 unsampled by the moorings.

827
828 Once clean time series were available to operate on, the energies and energy fluxes
829 were computed from the data via established techniques [Nash et al., 2005, 2006;
830 Lee et al., 2006]. The baroclinic velocity and pressure fluctuations induced by the
831 waves were first computed as

832
833
$$\bar{u}'(z,t) = \bar{u}(z,t) - \bar{u}(z) - \frac{1}{H} \int_{-H}^0 [\bar{u}(z,t) - \bar{u}(z)] dz \quad (1)$$

834
835 and
836

837
$$p'(z,t) = g \int_z^0 \rho'(\xi,t) d\xi - \frac{g}{H} \int_{-H}^0 \int_z^0 \rho'(\xi,t) d\xi dz \quad (2)$$

838
839 where

840
841
$$\rho'(z,t) = \rho(z,t) - \bar{\rho}(z) \quad (3)$$

842
843 is the density anomaly with respect to the time-mean density profile. In equations
844 (1) and (2), the last term satisfies the baroclinicity requirement that the primed
845 quantities integrate to zero over the entire water column [Kunze, et al., 2002]. Over
846 bars indicate temporal means. The HKE and APE can then be computed as

847
848
$$HKE = \rho_0 (u'^2 + v'^2) / 2 \quad (4)$$

849
$$APE = \frac{1}{2} \frac{g^2 \rho'^2}{\rho_0 N^2} \quad (5)$$



850

851 where ρ_0 is the mean density, g is the acceleration of gravity and N^2 is the buoyancy
852 frequency.

853

854 The energy flux due to highly nonlinear internal waves is given by

855

$$856 \quad \bar{F}_E = \bar{u}'(p' + HKE + APE) \quad (6)$$

857

858 where the first term on the right is the pressure work and the second and third
859 terms represent the advection of horizontal kinetic and available potential energy
860 density [Nash et al., 2012]. For the small amplitude, linear, hydrostatic case the flux
861 equation is often approximated as the first term only

862

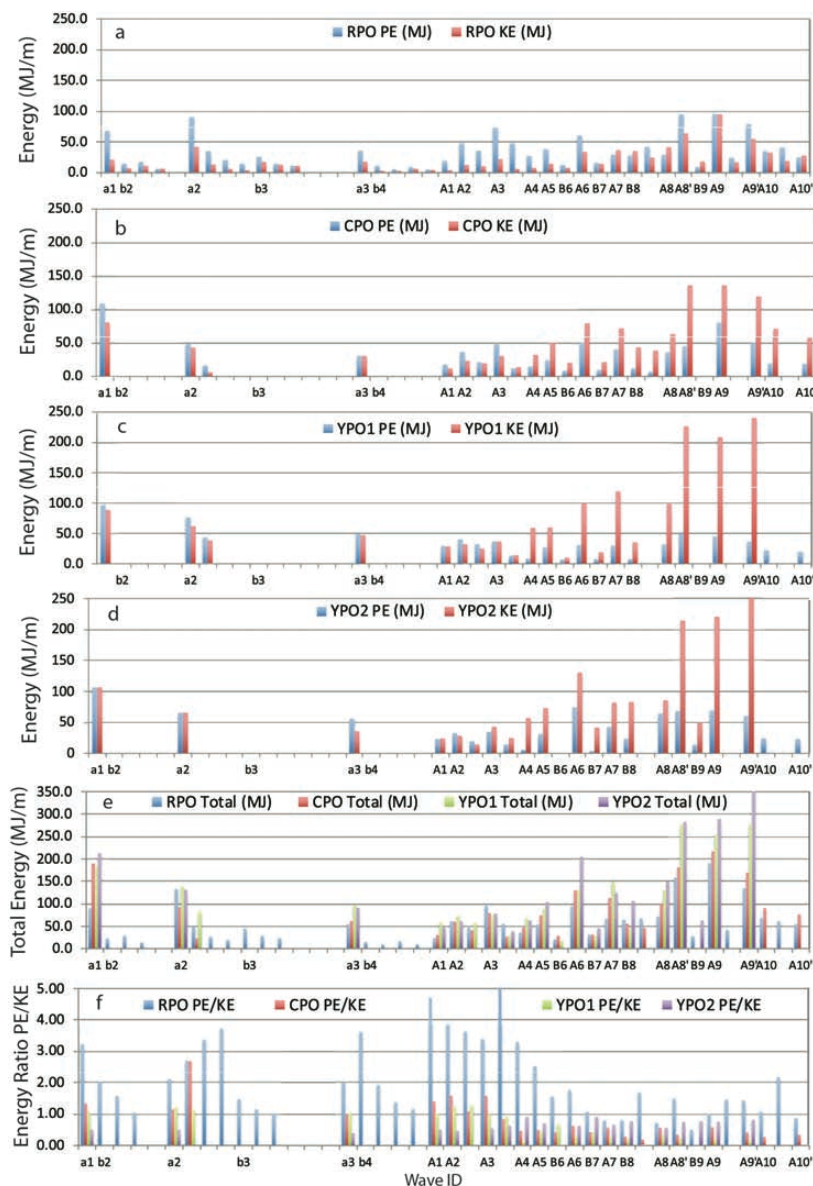
$$863 \quad \bar{F}_E = \bar{u}'p' \quad (7)$$

864

865 but since it is not obvious that this approximation is valid for the strongly nonlinear
866 shoaling waves observed in the sand dunes region, all three terms of the flux
867 equation were computed.

868

869 The resulting changes in the wave energy distribution across the slope depended on
870 the wave amplitude (Figure 15). For waves up to and including A3 on June 11, the
871 APE exceeded HKE offshore and continued to increase up the slope. This is
872 interpreted to mean the waves were still growing and had not yet reached
873 maximum amplitude. Smaller waves can penetrate farther upslope adiabatically
874 than larger waves. Wave A4 was anomalously small for which no obvious
875 explanation has been found. Perhaps the wave was obliterated by the leading edge
876 of tropical storm Hagabus. Starting with wave A5 on June 13, as the remote
877 barotropic tidal forcing continued to increase, the HKE exceeded APE at YPO2 by a
878 factor averaging 1.7 and increased to its maximum value at mooring CPO. This ratio
879 is even larger than the theoretical expectation of 1.3 [Turkington 1991; Lamb and
880 Nguyen, 2009] and indicates highly nonlinear waves with large amplitudes.
881 Between CPO and RPO, there was a dramatic change when the APE increased and
882 the HKE sharply decreased, resulting in greater APE than HKE at mooring RPO
883 (Figure 15f). The energy ratio at RPO (Figure 15f) was commonly three to four but
884 suddenly decreased sharply with the arrival of wave A6 on June 14 and remained
885 near one for the remainder of the time series. This is attributed to the increased
886 surface mixed layer depth as the tropical storm went by which wiped out the upper
887 ocean stratification and reduced the APE. The total energies (Figure 15e) integrated
888 both vertically and over a wavelength, followed an envelope consistent with the
889 remote tidal forcing and maxed out at around 200 MJ m^{-1} . This was less than half
890 the energy (550 MJ m^{-1}) previously reported over the Dongsha Plateau [Lien et al.,
891 2014] where the maximum observed wave amplitudes exceeded 150 m vs. 80 m
892 here. The total energy appears approximately conserved across the slope for many
893 of the waves as indicated by color bars of approximately equal length (Figure 15e).
894 The losses in HKE were compensated for by the increases in APE. There were



895
 896

897 *Figure 15. Energy transformations across the slope. The total HKE and APE,*
 898 *computed by integrating the wave energy both vertically and horizontally at moorings*
 899 *RPO, CPO, YPO1, and YPO2 are shown in panels a-d respectively. The total pseudo-*
 900 *energy (HKE + APE) at all four moorings is shown for each wave in panel e, and the*
 901 *APE/HKE ratio in panel f.*



902

903 exceptions however: wave a1 on June 3 and A7 on June 15 had much less energy
904 arriving at RPO than was present at CPO. This may have been due to tropical storm
905 Hagabus for the June 15 wave, but the reason is not obvious for the June 3 wave.
906 Altogether the results are consistent with the idea of greater HKE in the larger
907 incident waves with energy transferring from HKE to APE as the waves shoaled.
908 The results are in reasonable agreement with theory and numerical simulations
909 [Lamb and Nguyen, 2009; Lamb and Warn-Varnas, 2015].

910

911 In the simplest sense the energy flux is just the energy times the group velocity (or
912 phase velocity for non-dispersive waves). Since the phase velocity varied from 1.87
913 m s^{-1} between YPO2 and YPO1 to 1.69 m s^{-1} from CPO to RPO, the flux/energy ratio
914 is expected to vary little across the slope and the flux patterns should resemble that
915 of the total energies. This is indeed the case as seen by comparing the envelope of
916 the curves for the total flux (Figure 16a) and the total energy (Figure 15f). The
917 vertically integrated flux tends to decrease upslope primarily due to the decreasing
918 water depth. Of greater interest is the change in the various terms of equation (6).
919 The pressure work is indeed the largest term but not by much: The PW comprised
920 57%, 56%, 43%, and 52% of the total flux at YPO2, YPO1, CPO, and RPO
921 respectively. The large percentage still remaining was accounted for by the
922 advection of HKE and APE and shows that the waves were indeed strongly
923 nonlinear. The increase in APE with respect to HKE at mooring RPO versus CPO can
924 be accounted for by the change in the fluxes at those moorings (Figure 16b). From
925 CPO to RPO, the kinetic energy flux dropped by 50% (blue line to green line) while
926 the potential energy flux went up slightly (red line to purple line).

927

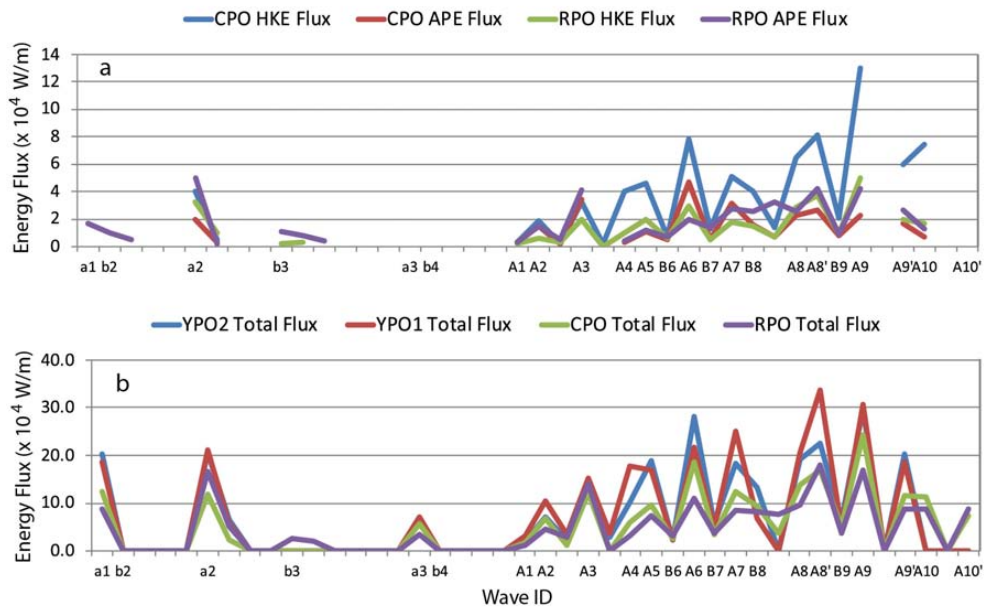
928 **5. Summary and conclusions**

929

930 A fortnight's worth of high-resolution velocity and temperature data were obtained
931 at four closely spaced moorings spanning 386-266 m depth on the continental slope
932 160 km northeast of Dongsha Island in the South China Sea. The experiment was
933 motivated by the need to understand ocean variability and how it interacts with
934 large (15 m) sand dunes on the sea floor and acoustic propagation. The dominant
935 signal observed was sets of large amplitude nonlinear internal waves (NLIWs,
936 sometimes also called solitons) impinging on the continental slope from the
937 southeast. These were in fact the very same waves that impact the Dongsha Island
938 region and have been reported by many previous authors. The "sand dunes" waves
939 however were about 50% smaller and less energetic than the "Dongsha" waves,
940 since the location was near the northern extremity of the wave crests rather than
941 near the center of the waves. The mean bottom slope along the sand dunes mooring
942 line was also gentler than farther southwest. While the internal tides are no doubt
943 important to the dune-building process, this paper focuses entirely on the NLIW
944 properties, most especially how the waves were transformed as they shoaled up a
945 very gradual bottom slope. New information gleaned includes the packet formation
946 process, further insights on the difference between a-waves and b-waves, and the
947 energy transformation processes which take place under wave shoaling.



948
949



950
951

952 *Figure 16. The energy flux up the slope for each of the nonlinear internal waves*
953 *identified in the sand dunes moored array data. a) The kinetic and potential energy*
954 *flux for moorings CPO and RPO. b) The total energy flux for all four moorings. This is*
955 *the sum of the kinetic, potential, and pressure work terms.*

956

957 During the fortnight observed, the a-waves began arriving several days ahead of the
958 b-waves and traveled in a more northerly direction. Once they started arriving, the
959 b-wave always lead the a-wave by 6-8 hours. In any given pair, the a-wave was
960 generally larger, but b-waves generated near spring tide may be larger than a-waves
961 generated near neap. The b-waves may also form packets, so that wave amplitude
962 and packet structure are not non-ambiguous ways to classify these waves. Rather,
963 the wave generation mechanism and their positioning relative to each other and the
964 internal tide determines the wave classification. The wave arrival patterns
965 rigorously track the tidal structure in Luzon Strait, even to the point of shifting by
966 six hours when the strong beat/weak beat pattern reversed in the strait during neap
967 tide. The b-waves were located near the head of the upslope internal tide while the
968 a-waves developed more towards the back. While it is tempting to ascribe the a-
969 wave formation to the ebb tide in the strait, released when the tide turned, and the
970 b-waves to the previous flood, the generation process is likely three-dimensional
971 and cannot be discerned from this far-field data set. A conundrum remains the
972 arrival of two large a-waves with nearly equal amplitude separated by two hours



973 during the period of maximal tidal forcing. Additional work is needed to understand
974 the origin of these waves.

975
976 At least two packet-generating mechanisms were clearly observed. Most a-waves
977 had already formed in the deep basin by the time they were incident upon the most
978 offshore mooring, YPO2 at the 388 m isobath. The behavior of these waves
979 depended on their amplitude: waves smaller than about 50 m and 100 MJ m^{-1}
980 propagated adiabatically upslope with little change of form. Waves larger/more
981 energetic than this formed packets via wave dispersion. Wave breaking was not
982 observed at any time, with the possible exception of the largest wave that was
983 steepening on the backside at the shallowest mooring, RPO at 266 m depth. The
984 waves likely break, and/or reflect, inshore of 266 m where the bottom is also
985 steeper. On the other hand, some of the b-waves were incident on YPO2 while
986 others were absent at YPO2 and formed while the internal tide shoaled between
987 YPO2 and RPO. These waves and wave packets were formed by the breaking of the
988 leading, strongly convergent edge of the upslope-propagating internal tide (not to
989 be confused with a breaking NLIW). This process took place right at mooring CPO
990 where a 5°C temperature front was nearly vertical. This process occurred just once
991 per day and was most easily discerned by the downslope tidal current near the
992 bottom which was not complicated by upper ocean processes.

993
994 The energy transformations also depended on wave amplitude. For the smaller
995 waves, the incident APE was greater than the HKE and continued to grow upslope.
996 For the larger waves, the incident HKE was larger than the APE, but the flux of HKE
997 decreased sharply upslope especially between 342m to 266 m, while the flux of APE
998 in that depth range increased slightly, resulting in greater APE than HKE farther
999 onshore. These results are in rough agreement with recent theory and numerical
1000 simulations of shoaling waves.

1001
1002 Important scientific issues still remaining to be studied include the how the internal
1003 tides and waves impact the dune formation process, determining the source and
1004 generation mechanisms for the a-waves vs. the b-waves, and understanding the
1005 double a-wave phenomenon near spring tide. These topics are the subject of other
1006 works in progress.

1007
1008



1009 **Acknowledgements**

1010

1011 This work was supported by the U.S. Office of Naval Research (ONR) under grant
1012 N000141512464 and by the Taiwan Ministry of Science and Technology (MOST).
1013 Wen-Hwa Her (IONTU) and Marla Stone (NPS) led the mooring work at sea. We
1014 thank the officers and crew of the research vessels OCEAN RESEARCHER 1, OCEAN
1015 RESEARCHER 3, and OCEAN RESEARCHER 5.

1016

1017

1018



1019 **References**

1020

1021 Alford, M. H., Lien, R.-C., Simmons, H., Klymak, J., Ramp, S. R., Yang, Y.-J., Tang, T.-Y.,
1022 Farmer, D., and Chang, M.-H.: Speed and evolution of nonlinear internal waves
1023 transiting the South China Sea, *J. Phys. Oceanogr.*, 40, 1338-1355, 2010.

1024

1025 Alford, M. H., MacKinnon, J. A., Nash, J. D., Simmons, H., Pickering, A., Klymak, J. M.,
1026 Pinkel, R., Sun, O., Rainville, L., Musgrave, R., Beitzel, T., Fu, K.-H., and Lu, C.-W.:
1027 Energy flux and Dissipation in Luzon Strait: Two tales of two ridges, *J. Phys.*
1028 *Oceanogr.* 41, 2211-2222, 2011.

1029

1030 Alford, M. H., Peacock, T., and co-authors: The formation and fate of internal waves
1031 in the South China Sea, *Nature*, 521, 65-69, 2015.

1032

1033 Buijsman, M. C., Kanarska, Y., and McWilliams, J. C.: On the generation and evolution
1034 of nonlinear internal waves in the South China Sea, *J. Geophys. Res.-Oceans*, 115,
1035 C02012, doi:10.1029/2009JC005275, 2010a.

1036

1037 Buijsman, M. C., McWilliams, J. C., and Jackson, C. R.: East-west asymmetry in
1038 nonlinear internal waves from Luzon Strait, *J. Geophys. Res.-Oceans*, 115, C1057,
1039 doi:10.1029/2009JC006004, 2010b.

1040

1041 Chang, M.-H., Cheng, Y.-H., Yang, Y.-J., Jan, S., Ramp, S. R., Reeder, D. B., Hseih, W.-T.,
1042 Ko, D. S., Davis, K. A., Shao, H.-J., and Tseng, R.-S.: Direct measurements reveal
1043 instabilities and turbulence within large amplitude internal solitary waves beneath
1044 the ocean, *Communications Earth & Environments*, 2, doi:10.1038/S43247-020-
1045 00083-6, 2021.

1046

1047 Chen, Y.-J., Ko, D. S., and Shaw, P.-T.: The generation and propagation of internal
1048 solitary waves in the South China Sea, *J. Geophys. Res.-Oceans*, 118, 6578-6589,
1049 doi:10.1002/2013JC009319, 2013.

1050

1051 Du, T., Tseng, Y.-H., and Yan, X.-H.: Impacts of tidal currents and Kuroshio intrusion
1052 on the generation of nonlinear internal waves in Luzon Strait, *J. Geophys. Res.-*
1053 *Oceans*, 113, C08015, doi:10.1029/2007JC004294, 2008.

1054

1055 Duda, T. F., Lynch, J. F., Irish, J. D., Beardsley, R. C., Ramp, S. R., Chiu, C.-S., Tang,
1056 T.-Y., and Yang, Y.-J.: Internal tide and nonlinear internal wave behavior at the
1057 continental slope in the northern South China Sea, *IEEE/J. Oc. Eng.*, 29, 1105-
1058 1131, 2004.

1059

1060



- 1061 Egbert, G., and Erofeeva, S.: Efficient inverse modeling of barotropic ocean tides,
1062 J. Atmos. Oceanic Technol., 19, 183-204, 2002.
1063
1064 Farmer, D., Li, Q., and Park, J.-H.: Internal wave observations in the South China Sea:
1065 The role of rotation and non-linearity, Atmosphere-Ocean, 47, 267-280, 2009.
1066
1067 Grimshaw, R., Guo, C., Helfrich, K., and Vlasenko, V.: Combined effect of rotation and
1068 topography on shoaling oceanic internal solitary waves, J. Phys. Oceanogr., 44, 1116-
1069 1132, 2014.
1070
1071 Jackson, C. B.: An empirical model for estimating the geographic location of
1072 nonlinear internal solitary waves, J. Atmos. Oceanic Technol., 26, 2243-2255, 2009.
1073
1074 Klymak, J. M., Pinkel, R., Liu, C.-T., Liu, A. K., and David, L.: Prototypical solitons in
1075 the South China Sea, Geophys. Res. Lett., 33, L11607,
1076 doi:10.1029/2006GL025932, 2006.
1077
1078 Kunze, E., Rosenfeld, L. K., Carter, G. S, and Gregg, M. C.: Internal waves in
1079 Monterey Submarine Canyon, J. Phys. Oceanogr., 32, 1890-1913, 2002.
1080
1081 Lamb, K. G.: A numerical investigation of solitary internal waves with trapped
1082 cores formed via shoaling, J. Fluid Mech., 451, 109-144, 2002.
1083
1084 Lamb, K. G., and Nguyen, V. T.: Calculating energy flux in internal solitary waves with
1085 an application to reflectance, J. Phys. Oceanogr., 39, 559-580, 2009.
1086
1087 Lamb, K. G., and Warn-Varnas, A.: Two-dimensional numerical simulations of
1088 shoaling internal solitary waves at the ASIAEX site in the South China Sea, Nonlin.
1089 Processes Geophys., 22, 289-312, 2015.
1090
1091 Lee, C. M, Kunze, E., Sanford, T. B., Nash, J. D., Merrifield, M. A., and Holloway, P.
1092 E.: Internal tides and turbulence along the 3000-m isobath of the Hawaiian
1093 Ridge, J. Phys. Oceanogr., 36, 1165-1183, 2006.
1094
1095 Li, Q., and Farmer, D. M.: The generation and evolution of nonlinear internal
1096 waves in the deep basin of the South China Sea, J. Phys. Oceanogr., 41, 1345-
1097 1363, 2011.
1098
1099 Lien, R. C., D'Asaro, E. A., Henyey, F., Chang, M. H., Tang, T. Y. and Yang, Y.-J.:
1100 Trapped core formation within a shoaling nonlinear internal wave, J. Phys.
1101 Oceanogr., 42, 511-525 2012.
1102
1103
1104



- 1105 Lien, R. C., Henyey, F., Ma, B., and Yang, Y. J.: Large-amplitude internal solitary
1106 waves observed in the northern South China Sea: Properties and Energetics, *J.*
1107 *Phys. Oceanogr.*, 44, 1095-1115, 2014.
1108
1109 Liu, A. K., Ramp, S. R., Zhao, Y., and Tang, T. Y.: A case study of internal solitary wave
1110 propagation during ASIAEX 2001, *IEEE/J. Oc. Eng.*, 29, 1144-1156, 2004.
1111
1112 Moum, J. N., Klymak, J. M., Nash, J. D., Perlin, A., and Smyth, W. D.: Energy
1113 transport by nonlinear internal waves, *J. Phys. Oceanogr.*, 37, 1968-1988, 2007.
1114
1115 Nash, J. D., Alford, M. H., and Kunze, E.: Estimating internal wave energy fluxes in the
1116 ocean, *J. Atm. and Oc. Tech.*, 22, 1551-1570, 2005.
1117
1118 Nash, J. D., Kunze, E., Lee, C. M., and Sanford, T. B.: Structure of the baroclinic tide
1119 generated at Kaena Ridge, Hawaii, *J. Phys. Oceanogr.*, 36, 1123-1135, 2006.
1120
1121 Nash, J. D., Kelly, S. M., Shroyer, E. L., Moum, J. N., and Duda, T. F.: The unpredictable
1122 nature of internal tides on the continental shelf, *J. Phys. Oceanogr.*, 42, 1981-2000,
1123 2012.
1124
1125 Orr, M. H., Mignerey, P. C.: Nonlinear internal waves in the South China Sea:
1126 Observations of the conversion of depression internal waves to elevation internal
1127 waves, *J. Geophys. Res.* 108, 3064, doi:10.1029/2001JC001163, 2003.
1128
1129 Ramp, S.R., Chiu, C. S., Kim, H.-R., Bahr, F. L., Tang, T.-Y., Yang, Y. J., Duda, T., and
1130 Liu, A. K.: Solitons in the Northeastern South China Sea Part I: Sources and
1131 Propagation Through Deep Water, *IEEE/J. Oc. Eng.*, 29, 1157-1181, 2004.
1132
1133 Ramp, S. R., Yang, Y. J., and Bahr, F. L.: Characterizing the nonlinear internal wave
1134 climate in the northeastern South China Sea, *Nonlin. Processes Geophys.*, 17, 481-
1135 498, doi:10.5194/npg-17-481-2010, 2010.
1136
1137 Ramp, S. R., Park, J.-H., Yang, Y. J., Bahr, F. L., and Jeon, C.: Latitudinal Structure of
1138 Solitons in the South China Sea, *J. Phys. Oceanogr.*, 49, 1747-1767, 2019.
1139
1140 Reeder, D. B., Ma, B., and Yang, Y. J.: Very large subaqueous sand dunes on the upper
1141 continental slope in the South China Sea generated by episodic, shoaling deep-water
1142 internal solitary waves, *Mar. Geol.*, 279, 12-18, 2010.
1143
1144 Scotti, A., Beardsley, R. C., and Butman, B.: On the interpretation of energy and
1145 energy fluxes of nonlinear internal waves: An example from Massachusetts Bay, *J.*
1146 *Fluid Mech.*, 561, 103-112, 2006.
1147



- 1148 Small, J.: A nonlinear model of the shoaling and refraction of interfacial solitary
1149 waves in the ocean. Part I: Development of the model and investigations of the
1150 shoaling effect, *J. Phys. Oceanogr.*, 31, 3163-3183, 2001.
1151
1152 Small, J.: A nonlinear model of the shoaling and refraction of interfacial solitary
1153 waves in the ocean. Part II: Oblique refraction across a continental slope and
1154 propagation over a seamount, *J. Phys. Oceanogr.*, 31, 3184-3199, 2001.
1155
1156 Turkington, B., Eydeland, A., and Wang, S.: A computational method for solitary
1157 internal waves in a continuously stratified fluid, *Stud. Appl. Maths.*, 85, 93-127,
1158 1991.
1159
1160 Vlasenko, V., Ostrovsky, V. L., and Hutter, K.: Adiabatic behavior of strongly
1161 nonlinear internal solitary waves in slope-shelf areas, *J. Geophys. Res.*, 110, C04006,
1162 doi:10.1029/2004JC002705, 2005.
1163
1164 Vlasenko, V., Guo, C., and Stashchuk, N.: On the mechanism of A-type and B-type
1165 internal solitary wave generation in the northern South China Sea, *Deep-Sea Res. I*,
1166 69, 100-112, 2012.
1167
1168 Vlasenko, V., and Stashchuk, N.: Three-dimensional shoaling of large-amplitude
1169 internal waves, *J. Geophys. Res.-Oceans*, 112, C11018, doi:10.1029/2007JC004107,
1170 2007.
1171
1172 Vlasenko, V., and Hutter, K.: Numerical experiments on the breaking of solitary
1173 internal waves over a slope-shelf topography, *J. Phys. Oceanogr.*, 32, 1779-1793,
1174 2002.
1175
1176 Yang, Y. J., Fang, Y. C., Chang, M.-H., Ramp, S. R., Kao, C.-C., and Tang, T.-Y.:
1177 Observations of second baroclinic mode internal solitary waves on the continental
1178 slope of the northern South China Sea, *J. Geophys. Res.-Oceans*, 114, C10003,
1179 doi:10.1029/2009JC005318, 2009.
1180
1181 Yang, Y. J., Fang, Y. C., Chang, Y.-T., Tang, T. Y., and Ramp, S. R.: Convex and concave
1182 types of second baroclinic mode internal solitary waves, *Nonlin. Processes*
1183 *Geophys.*, 17, 605-614, doi:10.5194/npg-17-605-2010, 2010.
1184
1185 Zhang, Z., Fringer, O. B., and Ramp, S. R.: Three-dimensional, nonhydrostatic
1186 numerical simulation of nonlinear internal wave generation and propagation in the
1187 South China Sea, *J. Geophys. Res.-Oceans*, 116, C05022, doi:10.1029/2010JC006424,
1188 2011.
1189
1190
1191